Solar Energy 296 (2025) 113563

Contents lists available at ScienceDirect

Solar Energy

journal homepage: www.elsevier.com/locate/solener

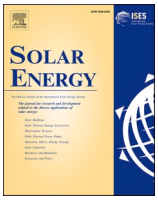

Experimental analysis of pre-startup, normal operation, and accident conditions for a megawatt-scale molten salt steam generation system

Xiang Liu [a], Fengyongkang Wu [a], Xue Xue [a], Yifan Zhu [a], Yaqiong Guo [b], Mingbao Zhang [b], Hao Zhou [a,*]

[a] Zhejiang University, Institute for Thermal Power Engineering, State Key Laboratory of Clean Energy Utilization, Hangzhou 310027, PR China
[b] Harbin Boiler Company Limited, Haerbin 150000, PR China

ARTICLE INFO

Keywords:
SGS
Efficiency
Accident condition
Heat exchange
Predictive model

ABSTRACT

MW-level pilot platform was derived from 100 MW solar thermal project, including preheater, evaporator, superheater and molten salt heater. Experiments were carried out under system pre-start, normal, and accident conditions. Results show that the steam/water side before the superheater must be preheated to operational temperature before introducing molten salt in natural circulation mode, as initial salt introduction causes significant thermal shocks to the tank walls. When the molten salt flow increases from 1 to 2 kg/s and temperature rises from 425 to 480 °C, the thermal efficiency of the heat exchangers decreases due to increased heat loss and worsening boiling conditions. Efficiency ranges for the preheater, evaporator, and superheater are 40–55 %, 80–95 %, and 50–65 %, respectively. Preheater and evaporator exhibit minimal thermal resistance (~0.0004 °C/W). While 90 % and 70 % of the total thermal resistance of the superheater and preheater are on the steam and molten salt sides, respectively. Failures in the molten salt heater, pump shutdown, and safety valve release significantly impact the superheater but have minimal effect on the preheater and evaporator. After heater failure, the temperature on the molten salt side of the superheater decreases by 1–2 °C/min, while the superheated steam temperature drops by 8–9 °C/min. When combined with pump stoppage, steam pressure decreases by 0.4 MPa/min, with the temperature dropping as fast as 16 °C/min. Overpressure range and prediction model were obtained based on measured data and statistical analysis. Findings will provide a theoretical basis for the design and operation of 100 MW class SGS.

1. Introduction

The integration of renewable energy technologies, such as solar thermal power tower generation and molten salt reactor nuclear power, offers practical strategies for achieving carbon neutrality [1,2]. With the rapid growth of renewable electricity, retrofitting coal-fired power plants to enhance flexibility by coupling with molten salt energy storage has become an essential pathway for all coal-fired units [3,4]. Molten salt heat exchanger, a critical energy conversion device in these systems, plays a vital role in ensuring the safe, stable, and efficient operation of the entire system. Heat exchanger system, which includes a preheater, evaporator, and superheater, converts the thermal energy of molten salt into high-temperature, high-pressure steam to drive turbines for electricity generation [5]. The complexity of various heat exchangers introduces significant challenges in the flow process of molten salt and the drastic changes in thermophysical properties. Therefore, conducting experimental research on megawatt-scale molten salt steam generation systems is essential for the large-scale engineering application of this technology [6].

Current research on the characteristics of molten salt heat exchange systems primarily focuses on the type of molten salt [7], the design of heat exchangers, and heat transfer enhancement [8]. The molten salts studied include FLiNaK [9], LiF-BeF_2-ThF_4-UF_4 [10], $NaBF_4$-NaF [11], $LiNO_3$ [12], $MgCl_2$-NaCl [13], and Solar Salt [14]. The dimensionless correlations of molten salts in transitional and turbulent flow regimes align well with the classical Dittus-Boelter [15] heat transfer model [16]. Further comparison of established models reveals that the temperature-dependent viscosity characteristics of different molten salts significantly influence their flow and heat transfer processes. Therefore, it is essential to utilize numerical simulations or experimental methods to clarify the properties of novel molten salts.

Developing novel and efficient molten salt heat exchangers is also a significant focus of current research [17]. Numerous dimensionless

* Corresponding author.
E-mail address: zhouhao@zju.edu.cn (H. Zhou).

https://doi.org/10.1016/j.solener.2025.113563
Received 28 November 2024; Received in revised form 11 April 2025; Accepted 26 April 2025
Available online 7 May 2025

Nomenclature

P1-4	System equipment pressure [MPa]
μ	Average kinetic viscosity [Pa·s]
Q	Mass flow rate [kg/s]
η	Thermal efficiency
S	Actual heat transfer area [m^2]
K	Overall convective heat transfer coefficient (OHTC) [W/(m^2 °C)]
Nu	Nussle number
D	Diameter of the shell side [m]
d	Inner diameter of tube [m]
Pr	Prandtl number
R	Thermal resistance [°C/W]
l	Length of a single tube [m]
d'	Outer diameters of tube [m]
T	Temperature [°C]
C_p	Specific heat capacity [J/(kg·°C)]
ρ	Average density [kg/m^3]
P	Power [W]
h	Enthalpy [J/kg]
q	Heat flux [W/m^2]
ΔT	Logarithmic mean temperature difference (LMTD) [°C]
hs	Convective heat transfer coefficient [W/(m^2·°C)]
D_e	Equivalent diameter [m]
N	Number of tubes
Re	Reynolds number
L	Characteristic length [m]
λ	Thermal conductivity [W/m·°C]

Subscript

re	release processes
s	molten salt
in	inlet
j	preheater, evaporator, and superheater
wa	Tube wall
c	Cold molten salt
ab	absorption processes
w	water/steam
out	outlet
f	fluid

models have been established to describe the heat transfer characteristics of different flow regimes in U-tube and conventional shell-and-tube heat exchangers [18]. Additionally, some researchers have explored the impact of baffle installation within heat exchangers on the heat transfer process, investigating various baffle designs such as bow-shaped [19], square-shaped [20], and rod baffles [6]. The results indicate that installing baffles causes the heat transfer characteristics of molten salts to deviate from classical heat transfer equations. The complexity introduced by forced convection necessitates further experiments or numerical simulations for different baffle types to identify the most appropriate correlation equations.

Several scholars have recently proposed various techniques to enhance heat transfer efficiency. These methods include replacing conventional heat transfer tubes with corrugated [21] or helical tubes [22], which have shown a 1.6–3.5 times increase in heat transfer performance. Other approaches include the addition of nanoparticles to molten salts, resulting in a 6.9 % to 19.3 % improvement [23], and the development of dual-stage molten salt systems [24].

In addition to focusing on individual heat exchangers or molten salts, some research teams have conducted more systematic studies. Team led by Sun Yat-sen University performed pilot-scale tests on the flow and heat transfer performance of saturated water within an integrated evaporator and superheater [25]. Their research revealed the impact of water flow rate, molten salt temperature, and flow rate on overall system efficiency. Results indicated that the thermal efficiency of the heat exchange system decreases with increasing molten salt temperature and flow rate, and that excessive wall superheat can lead to deteriorative boiling heat transfer [26]. Bi from Xi'an Jiaotong University, China [16] investigated the heat transfer characteristics between water/steam and molten salt at pressures exceeding 10 MPa [27]. Their findings showed that the heat transfer during boiling does not conform to traditional heat transfer models, and they developed experimental correlations for heat transfer between molten salt and boiling water [28]. Although there has been significant research on molten salt steam generation systems, there is a notable lack of experimental studies on fully integrated systems that couple preheater, evaporator, and superheater. Most existing research is concentrated in the academic realm, often overlooking critical issues encountered during actual operation. Based on the MW-level SGS experimental platform built in the laboratory (scaled down according to 100 MW on-site system), this work carries out the flow heat transfer study of the complete system of coupled preheater, evaporator, superheater, molten salt storage tanks, molten salt heaters, etc., and analyzes the pre-startup, normal operation, and accidental conditions. Results of the experiments can provide data support for the design, commissioning, and operation of a 100 MW-level SGS.

2. Experimental system and data processing

2.1. Description of the experimental system

As shown in Fig. 1, the pilot platform consists of three sections. On the left are the cold and hot salt storage tanks and the molten salt heater, which heats the cold salt to hot salt. On the right is the heat exchanger system, which includes three main components: preheater, evaporator, steam packet, and superheater. The central section comprises auxiliary components such as the soft water tank, water pump, molten salt pump, pre-feedwater heater, and drainage tank. Heat exchanger system was custom-designed and verified by Harbin Boiler Plant according to the experimental requirements, with the molten salt tank having a capacity of 450 L and constructed from 347H material. Molten salt heater operates using diesel fuel as a combustion heater. For further details on this component, refer to previous work [29]. The experiment involves two fluid circuits: the steam/water side and the molten salt side. High-temperature molten salt is pumped from the hot salt tank and flows sequentially through the superheater, evaporator, and preheater before entering the cold tank. Feedwater is pumped from the pre-feedwater heater, passing through the preheater, evaporator, and superheater in sequence. The molten salt's temperature decreases from 565 °C to 290 °C while the water is heated into superheated steam. The preheater raises the feedwater temperature close to saturation before it enters the evaporator, which is heated to produce saturated steam. This steam then flows into the superheater, which is heated into superheated steam. Finally, the cold salt is pumped into the cold salt tank, then to the molten salt heater for reheating, and subsequently delivered to the hot salt tank. Given the numerous temperature and pressure measurement points within the system, Fig. 1 illustrates the corresponding devices and the locations of the inlet and outlet of each measurement point for simplification in subsequent figures and tables.

Table 1 presents the design diagrams of the four main components in the heat exchange system. The preheater and evaporator are horizontal U-tube surface heaters to reduce thermal stress and increase the heat exchange area, while the superheater is designed as a hairpin-type heat

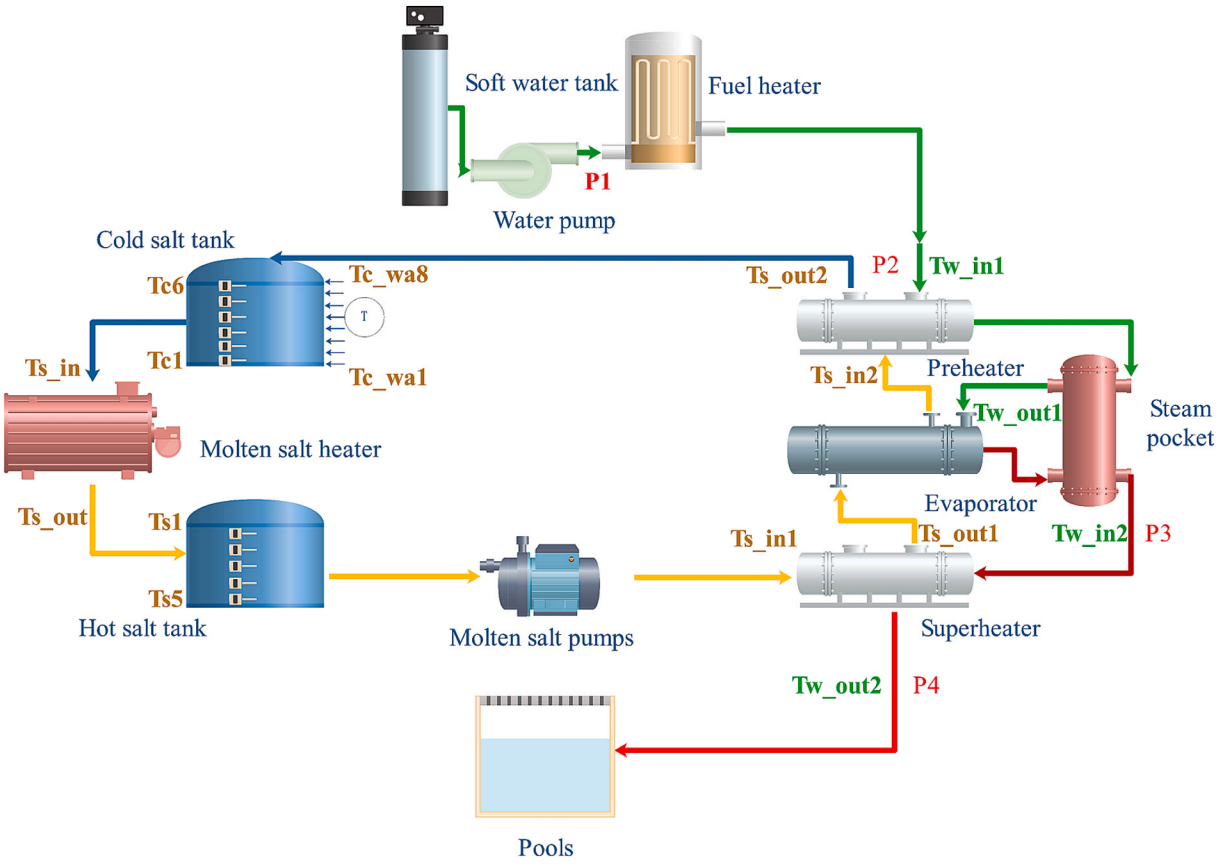

Fig. 1. Schematic Diagram of the System Flow and Key Parameter Measurement Points.

Table 1
Equipment structure parameters and materials.

Equipment project		Unit	Preheater YR-11	Evaporator ZF-20	Superheater GR-11	Steam-packet QB-0.2
Tube	Number	/	65	64	62	/
	OD	mm	14	14	14	/
	Thickness	mm	1.5	1.5	1.5	/
Total length of shell		mm	2503	4608	3663.5	3980
Inner diameter of shell		mm	299	356	201	407
Wall thickness of shell		mm	13	25	9	25
Water chamber diameter		mm	299	380	200	/
Water chamber wall thickness		mm	30	13	25	/
Thickness of tube plate		mm	85	70	75	/
Shell material		/	20	16Mn (IV)	SA-312TP347H	16Mn (IV)
Heat exchanger		/	20G	S34779	S34779	

exchanger. The total heat exchange areas of the preheater, evaporator, and superheater are 11 m^2, 20 m^2, and 17 m^2, respectively. In the preheater and superheater, the molten salt flows through the shell side, whereas in the evaporator, it flows through the tube side. The design pressure on the steam/water side is 9.9 MPa, while on the molten salt side, it is 1.2 MPa. The design temperatures for the shell side of the three heat exchangers are 350 °C, 350 °C, and 575 °C, respectively, with the tube side having 2, 4, and 1 passes. The steam packet has a design temperature of 350 °C, an adequate volume of 0.2 m^3, and a design pressure of 9.9 MPa. Its total volume is 0.47 m^3, with an operating temperature of 303.1 °C, a feedwater flow rate of 1.51 t/h, an operating pressure of 8.97 MPa, and a hydrostatic test pressure of 13.3 MPa.

The number of U-tubes in the preheater, evaporator, and superheater are 65, 64, and 62, respectively. The U-tubes have an outer diameter of 14 mm and a thickness of 1.5 mm. The tube center spacing is 19 mm in the longitudinal direction and 32.91 mm in the transverse direction, with a triangular arrangement. The tubes are connected to the tube sheet using a weld-first and then expansion process. The equipment's total length, shell diameter, and wall thickness are indicated in Table 1 and will not be repeated here. The steam generation system comprises 316 stainless steel, with a 7930 kg/m^3 density, specific heat of 502 kJ/kg·°C, and thermal conductivity described by λ (W/m·°C) = 15.02 + 0.01275T (°C). All heat exchange equipment is insulated with thermal cotton to minimize heat loss. Ternary molten salt Hitec was used in this study, which is a mixture composed of 53 % potassium nitrate (KNO_3), 40 % sodium nitrite ($NaNO_2$), and 7 % sodium nitrate ($NaNO_3$) by weight. The thermal properties were following [26]: specific heat C_p(J/kg·°C) = 2085 − 0.74T(°C), density ρ(kg/m^3) = 1549–0.15T(°C), thermal conductivity λ(W/m·°C) = 0.697 − 0.0000461T(°C), and viscosity μ(kg·$m^{-1}s^{-1}$) = 31.59 − 0.1948T + 0.0000425T^2 − 0.00000003133T^3(°C).

Fig. 2(a) shows the spatial arrangement of the four heat exchangers. The superheater is positioned at the highest level to ensure the molten salt flows naturally through all heat exchangers, and the preheater is at the lowest. The molten salt is pumped to the highest point of the system

(a) Layout of SGS appearance

(b) On-site installation of the superheater

(c) Hot salt tank

(d) The top of hot salt tank

Fig. 2. On-site layout of SGS and critical equipment.

(the superheater) and then flows downward by gravity. In addition, the material of the preheater is of lower quality compared to the superheater and other high-temperature equipment to save costs. This arrangement poses a significant issue: if the heat exchange system fails during operation, high-temperature molten salt may flow directly into the preheater, exceeding its maximum allowable working temperature and causing severe consequences. Only the evaporator and superheater use the same tube material (S34779), while the preheater employs a different material for its heat exchange tubes (20G) to save cost. The specific materials used are detailed in Table 1. Currently, the opposite spatial position is mainly used on-site, equipped with a molten salt pump to ensure the flow. Fig. 2(b) depicts the installation of the superheater before insulation material is applied. Fig. 2(c) and (d) show the front and top views of the molten salt tank, respectively. The tank is equipped with temperature measurement points inside and on the tank wall to monitor the temperature variations of the molten salt and the external wall.

The relative uncertainties corresponding to all the experimental sensors including molten salt flow meter, vapor/water flow meter, and high-temperature sensors are 0.02 %, 0.5 %, and 0.4 %, respectively. Based on the uncertainty calculation equations for indirectly measured physical quantities (2.2 Chapters), the relative uncertainties of all results in this study are shown in Table 2.

2.2. Model analyses

The calculation model for the power released by molten salt and absorbed on the steam/water side in the preheater, evaporator, and superheater is shown in Eq. (1). P represents power, W; Q denotes the mass flow rate of molten salt or water/steam, kg/s; C_p is the specific heat capacity of molten salt, J/kg·°C; T represents the temperature of the

Table 2
The relative uncertainties of all results.

Direct measurement	T	Qs	Qw
Uncertainty	0.4 %	0.02 %	0.5 %
Indirect measurement	P_{re}	P_{ab}	η
Uncertainty	0.4 %	0.64 %	0.74 %
Indirect measurement	q	ΔT	K
Uncertainty	0.64 %	0.57 %	0.86 %
Indirect measurement	Re	Nu	h_s
Uncertainty	0.02 %	0.63 %	0.63 %
Indirect measurement	R	R_s	R_w
Uncertainty	0.86 %	0.63 %	1.07 %

molten salt, °C; *h* denotes the enthalpy of water/steam, J/kg. Subscripts 're' and 'ab' correspond to the release and absorption processes, respectively; 's' and 'w' represent molten salt and water/steam, respectively; and 'in' and 'out' denote inlet and outlet. Variable 'j' can represent the preheater, evaporator, and superheater, respectively. The thermal efficiency η of the heat exchanger is given in Eq. (2).

$$P_{re,j} = Q_s C_p \left(T_{in,s,j} - T_{out,s,j}\right) P_{ab,j} = Q_w \left(h_{out,w,j} - h_{in,w,j}\right) \tag{1}$$

$$\eta_j = \frac{P_{ab,j}}{P_{re,j}} \tag{2}$$

Furthermore, the heat flux *q* can be calculated using Eq. (3) based on P_{ab} and the structural parameters of the heat exchanger, W/m^2; *S* represents each heat exchanger's actual heat transfer area, as previously provided, m^2. The calculation model for the logarithmic mean temperature difference ΔT is given in Eq. (4) [30,31], °C. Overall convective heat transfer coefficient *K* is determined using the model in Eq. (5), W/(m^2·°C). The convective heat transfer coefficient *hs* on the molten salt side in preheater and superheater is calculated using the model in Eqs. (6)–(8) and calculation method for h_s is determined using the Nu_s correlation [17], W/(m^2·°C). In these equations, λ denotes the thermal conductivity, W/m·°C; *Nu* stands for the Nusselt number; D_e represents the equivalent diameter of the heat exchange tubes in meters, m; D, N, d represent the diameter of the shell side, the number of tubes and inner diameter of tube; *Re* and *Pr* represent the Reynolds number and Prandtl number, respectively; μs and ρ_s represent the kinetic viscosity and density of molten salts at qualitative temperatures; *L* refers to the characteristic length of the heat exchange tubes in meters, m. 'f' and 'wa' represent the fluid viscosity corresponding to the qualitative temperature and wall temperature, respectively, Pa·s. Since the molten salt flows on the tube side of the evaporator, different dimensionless relational equations were chosen (9–10) to calculate *hs* [32,33].

$$q_j = \frac{P_{ab,j}}{S_j} \tag{3}$$

$$\Delta T_{in} = Ts\_in - Tw\_out \quad \Delta T_{out} = Ts\_out - Tw\_in \quad \Delta T_j = \frac{\Delta T_{in,j} - \Delta T_{out,j}}{\ln\left(\frac{\Delta T_{in,j}}{\Delta T_{out,j}}\right)} \tag{4}$$

$$K_j = \frac{q_j}{\Delta T_j} \tag{5}$$

$$D_{e,p} = \frac{\pi\left(D^2 - N{\cdot}d^2\right)}{\pi(D + N{\cdot}d)} = \frac{D^2 - Nd^2}{D + Nd} D_{e,s} = \frac{\pi\left(0.5D^2 - N{\cdot}d^2\right)}{\pi(0.5D + N{\cdot}d) + 0.5D} \tag{6}$$

$$\mathrm{Re} = \frac{\rho_s D_{e,j}}{\mu s} \cdot \frac{4Q_s}{\rho_s \pi\left(D^2 - N{\cdot}d^2\right)} \tag{7}$$

$$Nu_{s,j} = 1.61\left(\frac{\mathrm{Re}PrD_{e,j}}{L}\right)^{0.63}\left(\frac{\mu_f}{\mu_{wa}}\right)^{0.32} h_{s,j} = \frac{\lambda_s Nu_{s,j}}{D_{e,j}} \tag{8}$$

$$\mathrm{Re} = \frac{\rho_s d}{\mu s} \cdot \frac{4Q_s}{\rho_s \pi N d^2} \tag{9}$$

$$Nus,j = 1.86\left(\mathrm{Re}Pr\frac{d}{L}\right)^{1/3}\left(\frac{\mu_f}{\mu_{wa}}\right)^{0.14} h_{s,j} = \frac{\lambda_s Nu_{s,j}}{d} \tag{10}$$

The thermal resistance *R* analysis of the heat exchanger is shown in Eqs. (11)–(14). In these equations, d' represents the outer diameters of the heat exchange tubes; *l* indicates the length of a single heat exchanger tube, and *N* times *l* indicates the length of a single heat exchanger tube multiplied by the number of tubes. Using the previously obtained values of *K*, *q*, and ΔT, the thermal resistances on the water-side inside the heat exchanger (subscript 'w'), the tube wall (subscript 'wa'), and the molten salt side (subscript 's') can be calculated. Specifically, the total thermal resistance was first determined, which includes contributions from the molten salt side, tube wall, and water side, based on K and S. Subsequently, the thermal resistance on the molten salt side is calculated using hs and Eq. (12), while the tube wall resistance is obtained using Eq. (13). Finally, the water-side thermal resistance is derived by subtracting the molten salt and tube wall resistances from the total resistance.

$$R_j = \frac{1}{K_j \cdot S_j} = R_{w,j} + R_{wa,j} + R_{s,j} \tag{11}$$

$$R_{s,j} = \frac{1}{h_{s,j} \cdot S_j d'/d} \tag{12}$$

$$R_{wa,j} = \frac{1}{2\pi\lambda_{wa} N l} \ln\left(\frac{d'}{d}\right) \tag{13}$$

$$R_{w,j} = R_j - R_{s,j} - R_{wa,j} \tag{14}$$

3. Results and discussions

3.1. System startup process

Pilot-scale SGS involves numerous devices, and ensuring the safe and stable startup of the entire system is the first critical step for smooth operation. Figs. 3–5 illustrate the variations of various parameters as the system transitions from preparation to normal operation. Fig. 3 shows the flow rate of molten salt and the temperature changes on both the steam/water and the molten salt side within the main heat exchangers of the SGS. Tw_in1 and Tw_out2 were exposed to the external environment, which rose from 28 °C. Meanwhile, Tw_in2 and Tw_out1 are connected to the steam packet whose temperature remains consistently higher. Before starting the system, the steam/water side temperature must be increased, and circulation must start using the front feedwater preheater (0–14000 s). The temperatures on the steam/water side of the preheater, evaporator, and steam packet must reach above 250 °C to prevent the molten salt from freezing upon entering the system. There is a simultaneous drop in Tw_in1 and Tw_out1 at both ends of the preheater at 1000 s. In actual operation, there will be residual water in the preheater that was not completely drained from the last experiment. Due to better insulation, the temperature of the residual water drops slowly until the system is re-run and ambient water is introduced, the alternation between the high-temperature residual water and the ambient water results in a temperature drop. During this period, the temperature on the molten salt side within the equipment remains consistently above 300 °C. Combining electric tracing and high-temperature steam/water ensures complete thermal stability, thoroughly heating all equipment components. During the 0 to 14000 s period, water circulates through the preheater, evaporator, and steam drum. At this point, the diesel preheater is operating normally, gradually raising the water temperature. The feedwater flows from the preheater into the rising and descending pipes of the evaporator, where steam-water separation occurs in the rising pipe. The steam enters the steam drum, while the

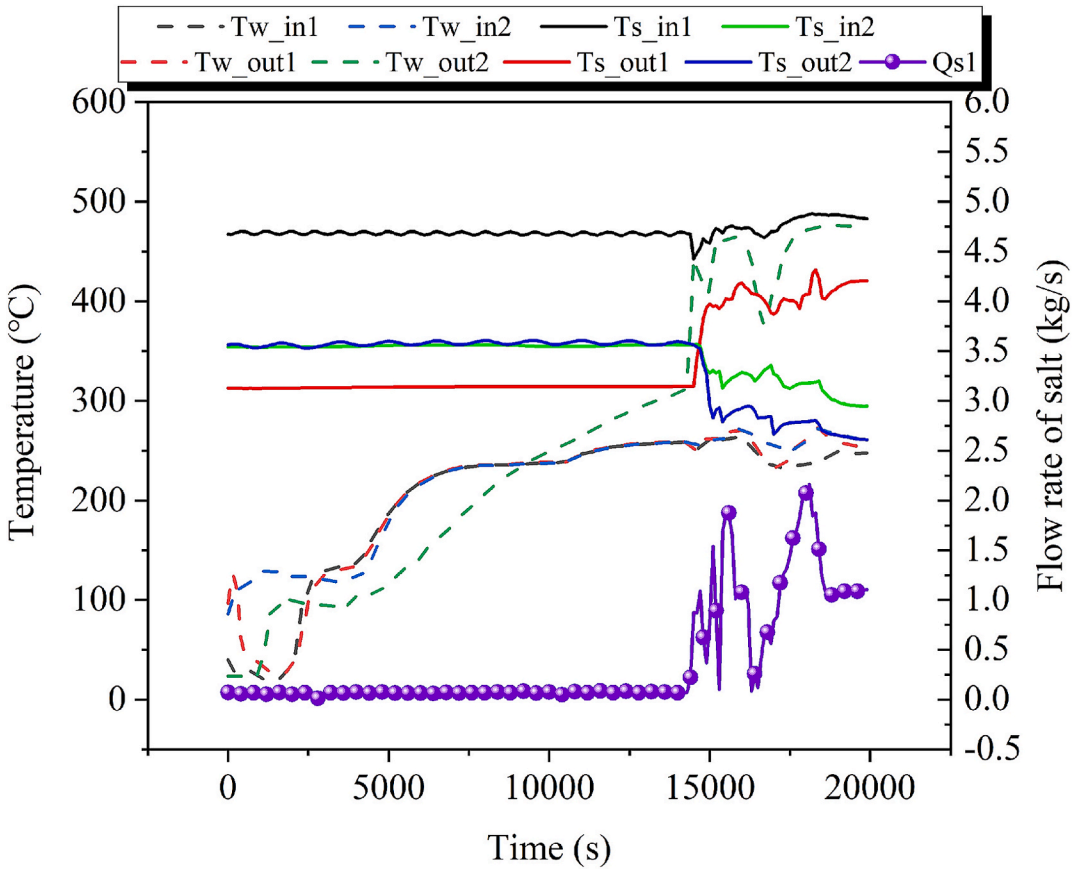

Fig. 3. Temperature and Flow Rate Variation Curves of Steam/Water and Molten Salt in the SGS System.

separated water and feedwater flow into the descending pipe to complete the circulation. The amount of steam generated in the evaporator during this phase is relatively low, and the liquid level balance in the steam drum is maintained by controlling the drainage valve to perform blowdown on the evaporator. The water/steam mass flow rates in the heat exchangers are not monitored. In this stage, the heat source for the preheater is provided by the diesel burner, while there is no heat source for the evaporator and superheater. The molten salt remains completely stationary during this phase. The molten salt flow rate jumped between 0–0.1 kg/s at 0–14000 s due to the acquisition error of the molten salt pump but did not flow. At 14,000 s, the molten salt pump is activated to introduce hot salt into the system, causing the inlet and outlet temperatures of the superheater to rise rapidly, followed by a swift increase in the outlet steam temperature. In the evaporator, molten salt releases substantial heat to vaporize the saturated water, causing Ts_in2 to decrease rapidly. Tw_in2 and Tw_out1, located within the evaporator and steam packet, respectively, remain at the saturation temperature corresponding to the operating pressure and do not experience significant changes. As the molten salt exits the evaporator and flows into the preheater, its temperature decreases to approximately 260 °C. Due to the large specific heat and latent heat of phase change of water, the temperature on the steam/water side is relatively stable during the preheating and evaporation stages, respectively, but increases rapidly during the superheating stage. The heat released from the molten salt is greatest in the evaporator, followed by the superheater, and is lowest in the preheater. In practice, Qs1 is controlled by adjusting the operating frequency of the molten salt pump, and the molten salt flow rate is adjusted based on the steam pressure and temperature at the outlet of the superheater. Therefore, the frequency of the molten salt pump is adjusted according to the outlet pressure and temperature of the steam side of the superheater, but due to the huge delay of the system, overadjustment often occurs, resulting in the fluctuation of Qs1 at the beginning of the experiment as shown in Fig. 3.

The front preheater for feedwater shares part of the preheating function, resulting in minimal temperature variation on the steam/water side at the inlet and outlet of the preheater. Additionally, the molten salt outlet valve must be closed for a while (Pressure holding) to ensure the molten salt fills all the heat exchanger tube bundles. As shown in Fig. 3, at 16,000 s, the molten salt flow rate drops to 0 and remains at this level for approximately 60 s before reopening the outlet valve. In addition, the other observed decrease in molten salt flow during 15,000 s and 16,000 s is primarily due to the large-scale nature of the system and the inherent delays associated with the control mechanisms. Specifically, the steam pressure and temperature at the superheater outlet are key factors controlling the molten salt pump flow. However, the system's delay response causes a mismatch in the flow control, leading to overcompensation by the molten salt pump, which results in the flow rate oscillating between increases and decreases. Finally, the molten salt flow rate is adjusted to 1 kg/s for the experiment. At this point, the steam/water side temperature increases from 220 °C to 450 °C, while the molten salt side temperature decreases from 470 °C to about 260 °C. The total time required for system preheating is approximately 6 h, with about 1 h for debugging after salt flow and approximately 5 h for the initial preparation of the steam/water side. The debugging operation during this period involves adjusting the molten salt pump flow rate based on the steam temperature and pressure at the superheater outlet to ensure the stability of these parameters. In addition to this key task, adjustments to the oil pump pressure for the preheater and the fuel supply to the molten salt heater are also carried out to maintain stable preheater outlet water temperature and molten salt inlet temperature. These fine-tuning steps are integral to the overall adjustment process and are continuously implemented throughout the commissioning phase.

Fig. 4 shows the pressure variation trends on the steam/water side of

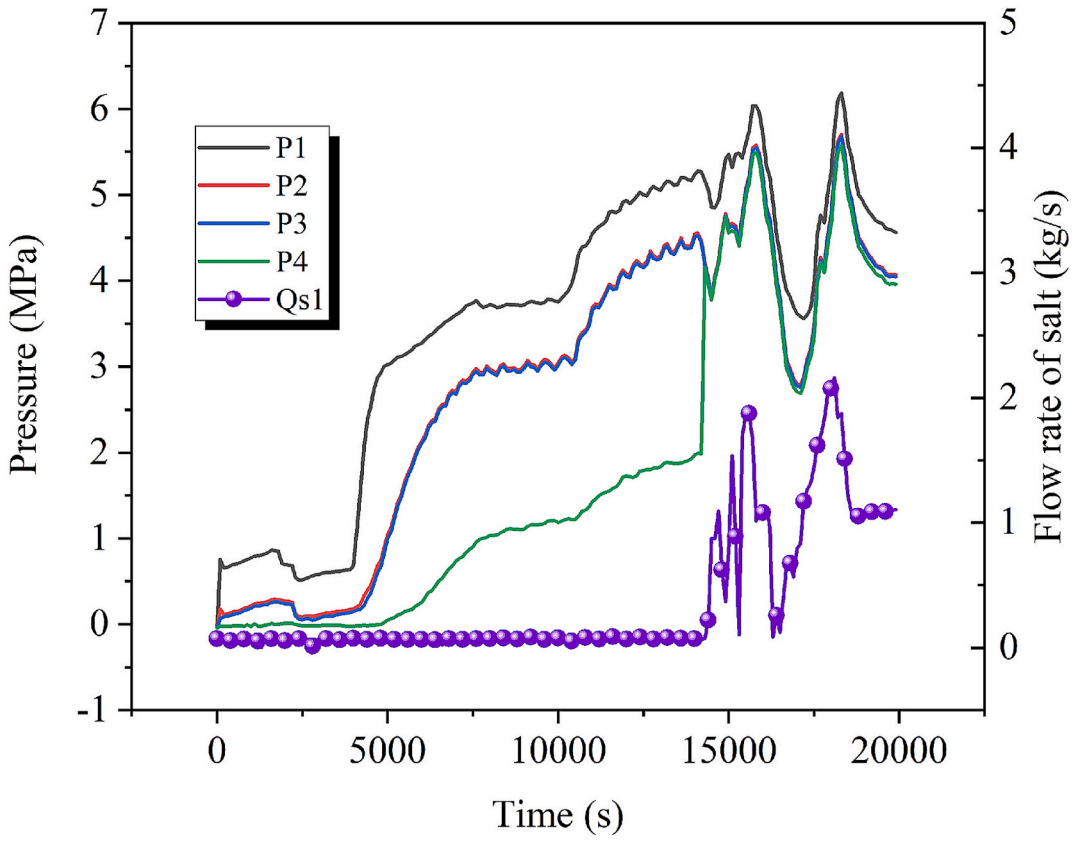

Fig. 4. Pressure Variation Curve on the Steam/Water Side in the SGS System.

the system. The pilot platform operates in a natural circulation mode. During the pre-start phase, the front preheater raises the water temperature to near the phase change point, after which steam/water separation occurs in the steam packet. At this point, the valve leading to the superheater is closed and the steam formed at the top of the packet is the main reason for maintaining high pressure on the steam/water side. However, achieving a completely tight seal is challenging in actual operation, resulting in a minor leakage of steam into the superheater. Furthermore, since the superheater outlet valve remained closed, the accumulated steam inside the superheater led to the observed increase in P4 pressure in Fig. 4. The pressure variations of P1, P2, and P3 are related to the preheating temperature of the feedwater, with the corresponding saturation pressure representing the operating pressure of the equipment at that moment. At 14,000 s, hot salt is introduced and the valve is opened, causing the pressure at the superheater outlet to rise rapidly. Steam pressure is closely tied to the steam temperature and flow rate. When the molten salt flow rate decreases, the steam temperature and generated steam flow rate also drop, leading to fluctuations in system pressure as the molten salt flow varies. Once the molten salt flow stabilizes at 1 kg/s, the pressure within the SGS system becomes steady at around 4 MPa. Given current production cost considerations, natural circulation is widely used in SGS systems, requiring operators to accurately control the molten salt flow to ensure stable steam output.

Fig. 5(a) shows the parameter variation trends during the startup process of the molten salt heater. The molten salt heater is a critical device connecting the cold and hot salt tanks. Cold salt tank is maintained at a temperature of 280 °C, while the hot salt tank is kept at 430 °C. It can be seen that Ts_in and Ts_out experience temperature oscillations at different frequencies. The molten salt storage tank is equipped with electric heating, which is activated or deactivated based on the set temperature. The temperature Ts_in reflects the cold salt temperature from the cold salt tank and exhibits oscillations due to the operation of its electric heater. Ts_out represents the temperature of hot salt exiting the molten salt heater. The observed oscillations are not caused by fluctuations in the burner oil flow, but rather by the presence of an electric heater installed at the outlet pipeline of the molten salt heater. This electric heater operates under a different power setting from that of the cold salt tank heater, resulting in distinct oscillation patterns. System is equipped with a cold salt pump that circulates cold salt into the molten salt heater coils, with the flow rate denoted as Qs1. A hot salt pump circulates hot salt into the SGS, with the flow rate denoted as Qs2. At 14,000 s, both molten salt pumps start operating with a flow rate of approximately 1.0–1.5 kg/s. During the initial system startup, heat exchange on the steam/water side is insufficient, causing the temperature of the cold salt discharged from the SGS to gradually decrease from 400 °C to around 320 °C. The liquid level in the cold salt tank mirrors the changes in Qs2, with an increase in Qs2 indicating a larger flow into the cold salt tank from the SGS, causing a rapid rise in the liquid level of the cold salt tank. During the pressure-holding operation, Qs2 drops to zero while Qs1 remains at a relatively high flow rate, causing the cold salt tank's liquid level to drop rapidly. Fig. 5(b) and (c) show the temperature distribution of the cold salt and the cold salt tank wall. Cold salt temperature fluctuates between 330 °C and 360 °C. While the tank wall has a minimum temperature of around 290 °C and a maximum of 360 °C, possibly exposed to air. It's worth noting that the sudden increase in Tc_6 and Tc_1 around 7000 s is caused by the activation of the electric heater inside the storage tank. The proximity of these two measurement points to the vicinity of the electric heater resulted in a sudden temperature rise. It can be seen that at this time the temperature of the hot salt also starts to rise in Fig. 5(d). Electric heating is applied to the molten salt in the storage tank before the experiment to prevent freezing and blockage. Fig. 5(d) illustrates the temperature distribution of the hot salt. At 14,000 s, the hot salt pump starts, decreasing the hot salt tank's liquid level and causing a rapid drop in Ts4 temperature. Subsequently, as hot salt from the molten salt heater outlet is transferred to the hot salt tank, the temperature at the tank's bottom (Ts1–Ts3)

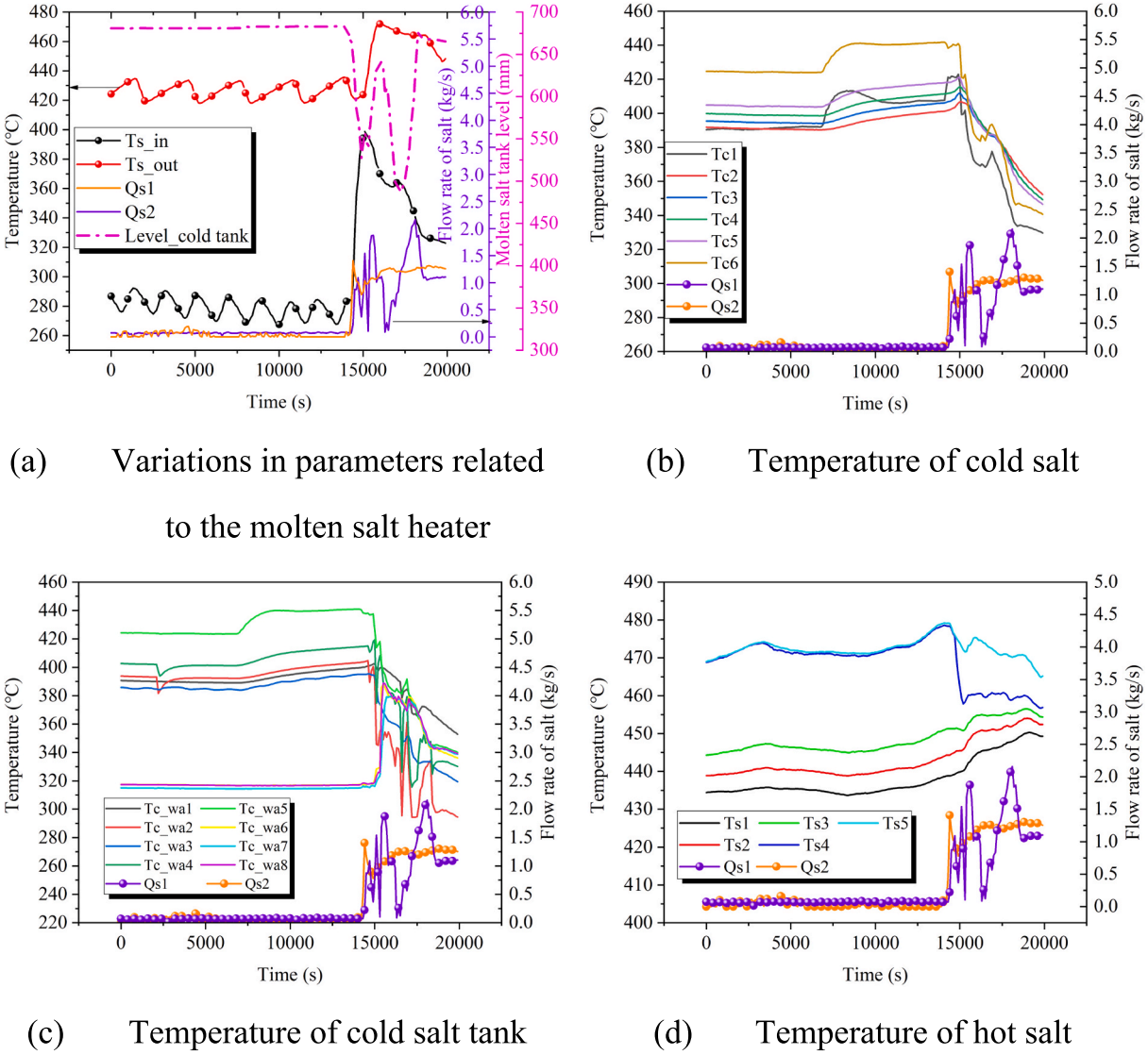

Fig. 5. Variation Curves of Parameters Related to the Molten Salt Heater and Storage Tank System.

gradually rises. The molten salt and tank wall temperatures tend to equalize as the operating time increases. In addition, the highest temperature appearing at the bottom of the storage tank is due to the internal heating coils designed to prevent freezing and blockage of molten salt. The inlet of the hot molten salt is located at the top of the tank, while the outlet is at the bottom. Before system operation begins, the bottom region maintains the highest temperature due to the localized effect of the heaters. Once the system starts, hot molten salt enters from the top, leading to a rapid temperature rise at the upper measuring point Ts1. From a thermal stress perspective, the molten salt tank experiences the greatest thermal non-uniformity during the initial startup phase, leading to the highest stress loads. Once the system stabilizes, the thermal conditions of the storage tank improve.

3.2. Impact of molten salt temperature and flow rate variations on system efficiency

Fig. 6(a) shows the trend of the log mean temperature difference (LMTD) of major equipment as the inlet salt temperature increases. As the molten salt temperature rises, the LMTD of the evaporator and superheater gradually increases [22]. The outlet temperature of the steam/water side of the evaporator remains consistent with the phase change point, thus showing minimal variation. It should be pointed out that the molten salt temperature shown in Fig. 6 refers to the inlet temperature for the entire system, specifically the inlet temperature at the superheater (Ts_in1). As the inlet salt temperature increases from 390 °C to 430 °C, the LMTD rises from 70 °C to 82 °C. The outlet temperature of the steam/water side of the superheater changes in line with the molten salt temperature, resulting in a slight increase in the superheater's average LMTD from 40 °C to 50 °C. The rise in LMTD leads to an increase in the overheating of the U-tube walls, effectively enhancing heat transfer and causing the overall heat transfer coefficient (OHTC) of the device to increase with the molten salt temperature. LMTD of the preheater initially increases and then decreases, which contradicts previous research findings [18,26]. At 480 °C, the hot salt entering the preheater has a temperature of 310 °C, while at 455 °C, it is 325 °C. At 455 °C, the evaporator pressure is 5.7 MPa, and the saturation temperature is 272.26 °C, but the measured internal temperature of the evaporator is 275 °C. This phenomenon indicates that the preheater heats subcooled water near or over the phase change point at 455 °C, thus taking on part of the evaporator's load. The reduced heat absorbed by the evaporator from the molten salt at 455 °C leads to an increase in the inlet salt temperature and LMTD of the preheater. The abnormal increase in the intermediate data leads to a change in the overall trend of

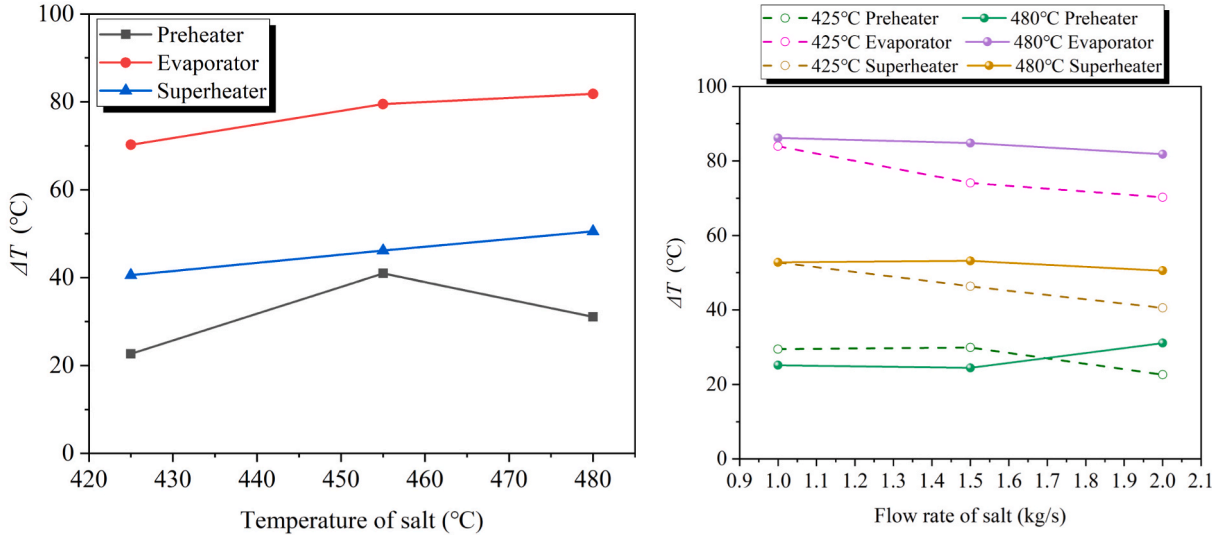

(a) The trend of the temperature difference with varying salt temperatures

(b) The trend of the temperature difference with varying salt flow rate

Fig. 6. Trend of Temperature Difference Across Heat Exchangers with Variations in Molten Salt Parameters.

LMTD. The preheater's higher outlet temperature is due to the higher temperature of the subcooled water entering from the front feedwater heater. Precise control of the front feedwater heater is crucial for maintaining the set efficiency of SGS equipment during field operation.

Fig. 6(b) shows the trend of the LMTD of the SGS device with varying molten salt flow rates. At 425 °C, the heat transfer temperature difference for the preheater, evaporator, and superheater shows a slight decreasing trend [25]. As the molten salt flow rate increases, the water temperature rises faster than the molten salt temperature, reducing the heat transfer temperature difference. At 480 °C, the heat transfer temperature differences for the evaporator and superheater are higher than those at 425 °C. However, the trend for the preheater at 480 °C differs from the others. As the inlet molten salt flow rate increases, the increasing rate in salt temperature surpasses that of the water temperature (limited by the phase change point), resulting in an increased heat transfer temperature difference. The variation in heat transfer temperature difference is a critical driver in the OHTC. Increasing the heat transfer temperature difference within a specific range results in a higher OHTC. However, excessive overheating of the tube walls can deteriorate boiling heat transfer, potentially reducing OHTC.

Fig. 7 shows the trend of thermal efficiency (η) of major equipment at 425 °C and 480 °C with varying molten salt flow rates. At 425 °C, the η of the hot salt decreases continuously with increasing molten salt flow rate. η of the evaporator is significantly higher than that of the superheater and preheater [18,26]. As the molten salt flow rate increases, the heat transfer coefficient between the hot salt and the heat exchanger wall increases, leading to a rapid rise in thermal losses within the heat

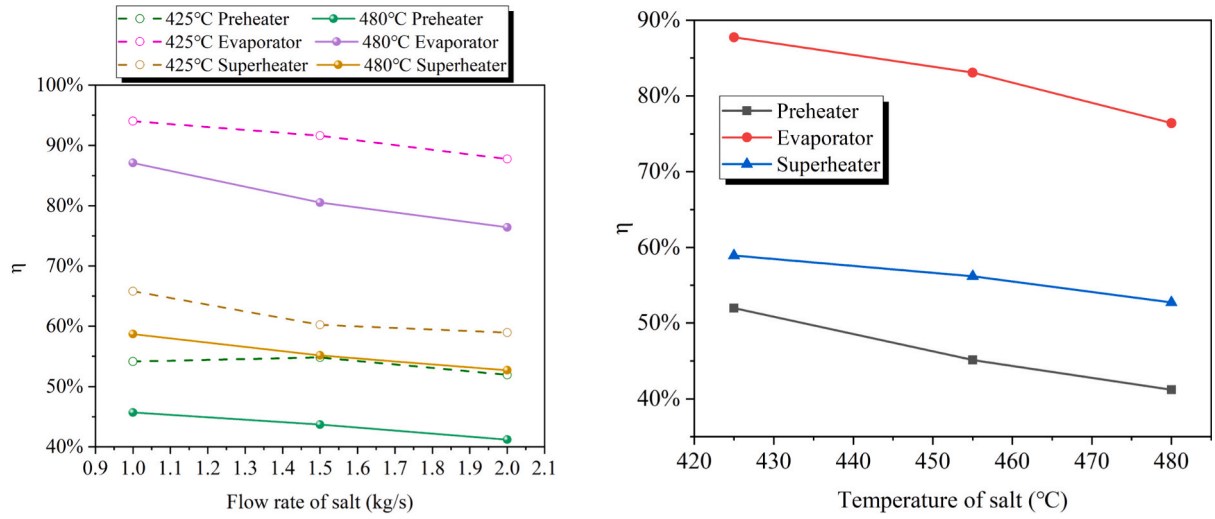

(a) The trend of η with varying salt flow rate

(b) The trend of η with varying salt temperatures

Fig. 7. Trend of η Across Heat Exchangers with Variations in Molten Salt Parameters.

transfer system and a consequent decrease in η. In this study, an additional fuel preheater was installed upstream of the preheater, effectively creating a two-stage preheating system. The preheater analyzed here corresponds to the second-stage heat exchanger between molten salt and water. Experimental observations indicate that the temperature rise in this section is relatively low because the first-stage preheater absorbs a significant portion of the preheating duty, while the second-stage preheater is limited by the phase change temperature, restricting further temperature increase and resulting in a lower η. The thermal efficiency of the evaporator remains relatively stable because its outlet temperature is fixed at the phase change point, causing almost no variation in the water/steam side outlet temperature. When the molten salt flow rate changes from 1 kg/s to 2 kg/s and temperature at 425 °C, the preheater, evaporator, and superheater efficiencies are 54 %–50 %, 94 %–89 %, and 64 %–61 %, respectively. At 480 °C and Qs1 changes from 1 kg/s to 2 kg/s and temperature at 425 °C, the thermal efficiency of the hot salt is lower compared to the 425 °C condition. This decrease is due to increased thermal losses in the system and potential worsening of boiling heat transfer caused by higher tube wall temperatures, which reduces the water-side capacity to absorb heat from the molten salt. The efficiency ranges for the preheater, evaporator, and superheater are relatively smaller at 45 %–40 %, 87 %–79 %, and 59 %–54 %, respectively. Overall, the evaporator has the highest thermal efficiency, varying between approximately 80 % and 95 % (Re: 700–2100), followed by the superheater, with an efficiency of around 50 %–65 % (Re: 600–2000), and the preheater with the lowest efficiency, ranging from 40 % to 55 % (Re: 300–900). Phase change heat transfer is superior to high-speed steam and forced convection heat transfer of subcooled water.

As the molten salt temperature increases, the heat loss in the evaporator and superheater rises significantly. While the growth in effective heat absorption slows, leading to a gradual decline in thermal efficiency. Additionally, the increase in the heat transfer temperature difference of the evaporator reduces the OHTC, causing the heat flux density to decrease accordingly. Furthermore, high superheat in the evaporator may lead to deteriorated boiling, further reducing thermal efficiency. Overall, for every 30 °C increase in the salt temperature of the preheater, evaporator, and superheater, the thermal efficiency decreases by approximately 5 %, 5 %, and 3 %, respectively. In industrial systems, overall thermal efficiency can be effectively improved by scaling up the system, enhancing insulation performance, and optimizing salt temperature and flow rate.

Fig. 8 illustrates the relationship between the heat flux density and Re for SGS heat exchange equipment. In the evaporator, the phase change results in the highest heat flux density, rapidly increasing with the molten salt flow rate, reaching up to 20 kW/m^2. The heat flux density in the superheater is about 3–10 kW/m^2 and shows an upward trend with the increase in molten salt flow rate. Although the Re of molten salt in the preheater is the lowest, the corresponding heat flux density is bigger than superheater due to better thermal conductivity and specific heat capacity, around 5–12 kW/m^2. Overall, the local heat flux density resulting from phase change heat transfer exceeds that of convective heat transfer involving steam and subcooled water.

Fig. 9 shows the trends of the convective heat transfer coefficient on the molten salt side(*hs*) and the OHTC with Re. The OHTC in the preheater shows considerable fluctuation, mainly due to the preheater heating the feedwater close to or over the phase change point. Although the feedwater absorbs most of the heat, its temperature barely changes, causing the LMTD to increase and OHTC to drop in regions of high Re consistent trend of heat flux density, ranging between 150 and 350 W/m^2·K. The evaporator exhibits the middle OHTC based on the largest LMTD and *q*, compared to the preheater and superheater. The highest local heat flux density and middle thermal resistance maintain the *hs* between 80 and 250 W/m^2·K. Fig. 9(c) shows the OHTC trend within the Re range of 600 to 2000, where the superheater reaches an OHTC of up to 250 W/m^2·K. Overall, heat flux density and the OHTC rise rapidly as

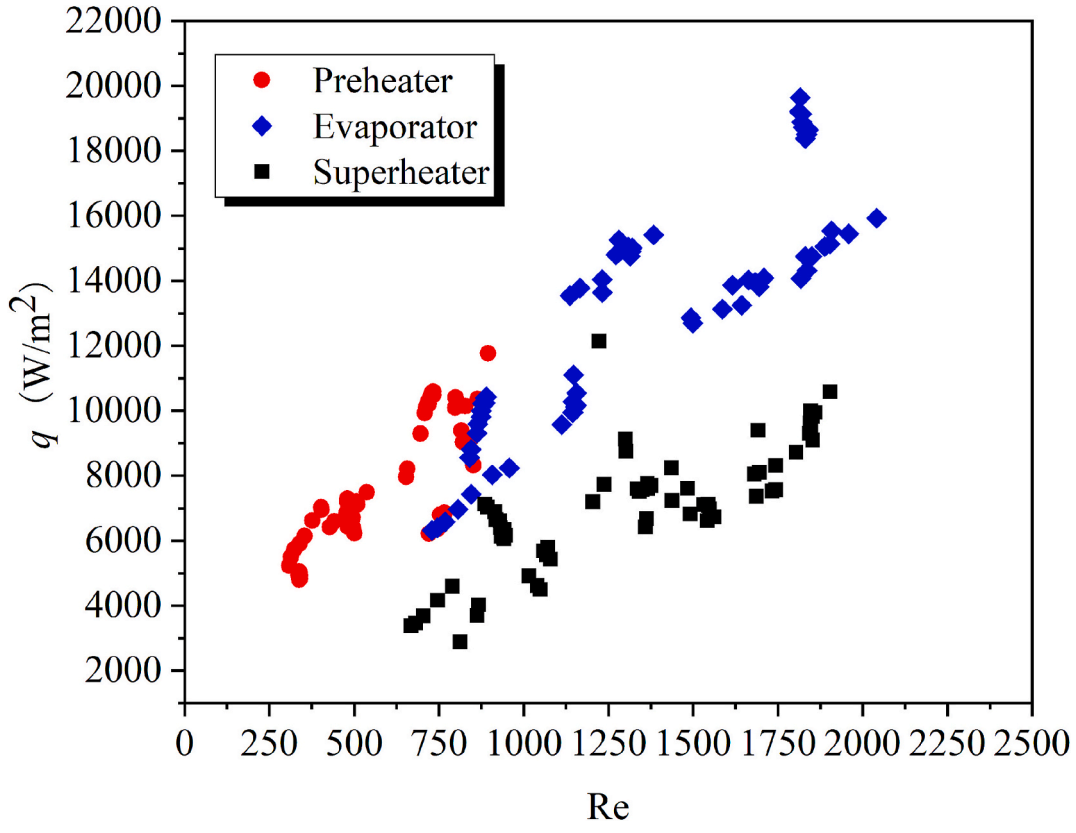

Fig. 8. Heat flux density curves for SGS equipment with varying molten salt Re.

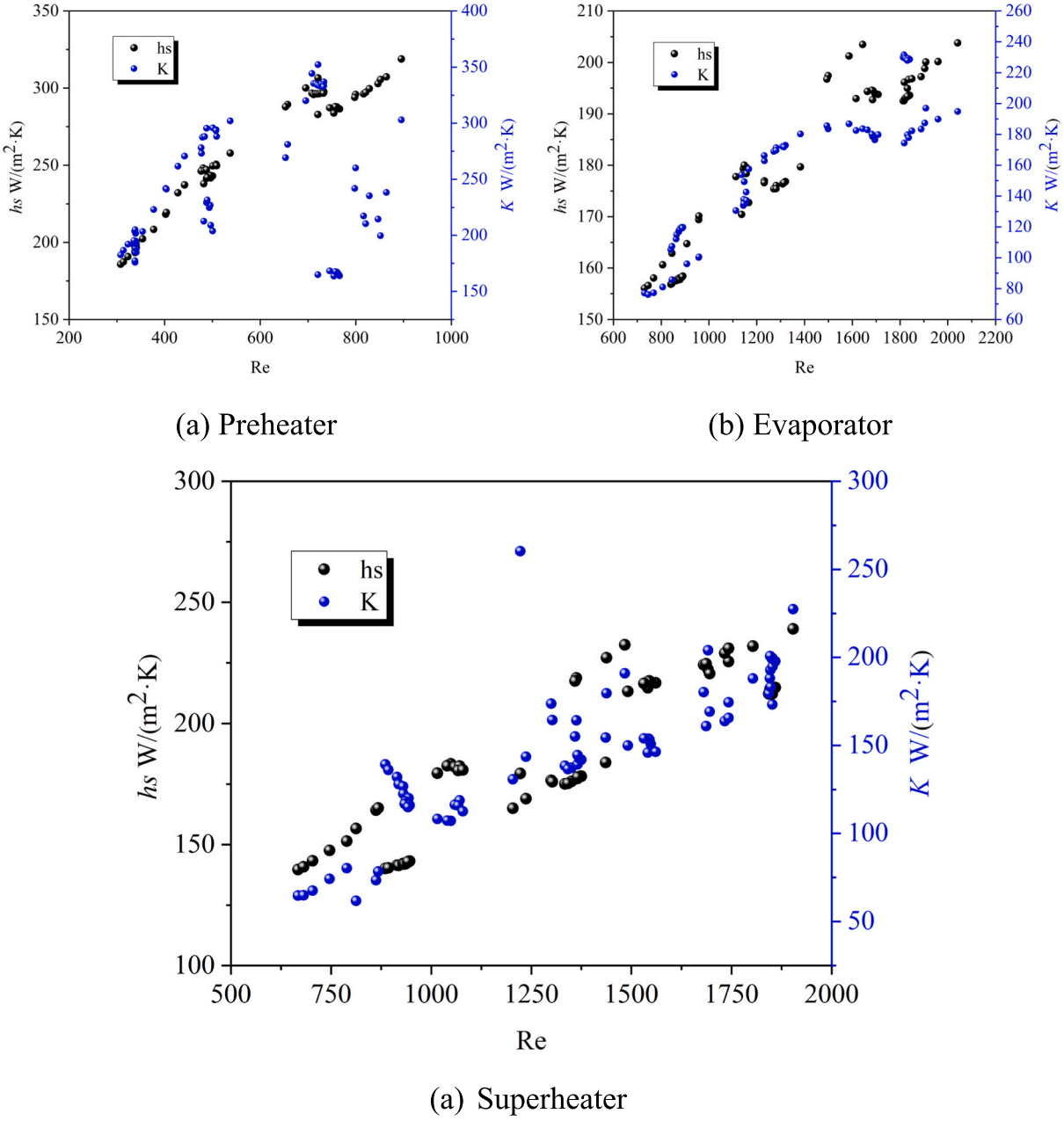

Fig. 9. The trends in *hs* and OHTC for the molten salt side with varying molten salt Re.

the Re of the molten salt increases. On the one hand, the increase in Re due to the higher molten salt temperature raises the wall to superheat, enhancing heat transfer. On the other hand, the higher flow velocity reduces thermal resistance and intensifies turbulence, resulting in more vigorous heat exchange.

Fig. 10 presents the variation in thermal resistance across different sections of the main equipment with increasing Re. Fig. 10(a) shows the evaporator and preheater have the lowest thermal resistance, followed by the superheater. The thermal resistance of the equipment decreases rapidly with the increase in Re, with the superheater exhibiting the fastest decline, which indicates that increasing the molten salt flow rate in the evaporator has the most significant effect on improving heat transfer. Fig. 10(b), (c), and (d) illustrate the thermal resistance distribution for the preheater, evaporator, and superheater. In the preheater, the thermal resistance on the molten salt side is 0.00025 °C/W, higher than the water-side resistance of 0.0001 °C/W, while the thermal resistance of the heat transfer surface is negligible. The water-side thermal resistance in the evaporator is smaller than that of the molten salt side (0.0002 °C/W), a pattern consistent with the preheater. The superheater has the highest water-side thermal resistance, approximately 0.00025 °C/W, accounting for over 50 % of the total thermal resistance. The evaporator follows, with a water-side thermal resistance of about 0.00015 °C/W, representing 40 % of the total. The preheater has the lowest water-side thermal resistance, about 25 % of the total. Therefore, heat transfer enhancement methods on the steam side of the superheater can effectively increase its OHTC and thermal efficiency [26]. Since the molten salt side in the preheater accounts for more than 70 % of the total thermal resistance, techniques like using corrugated pipes or installing baffles on the molten salt side can be employed to improve the OHTC.

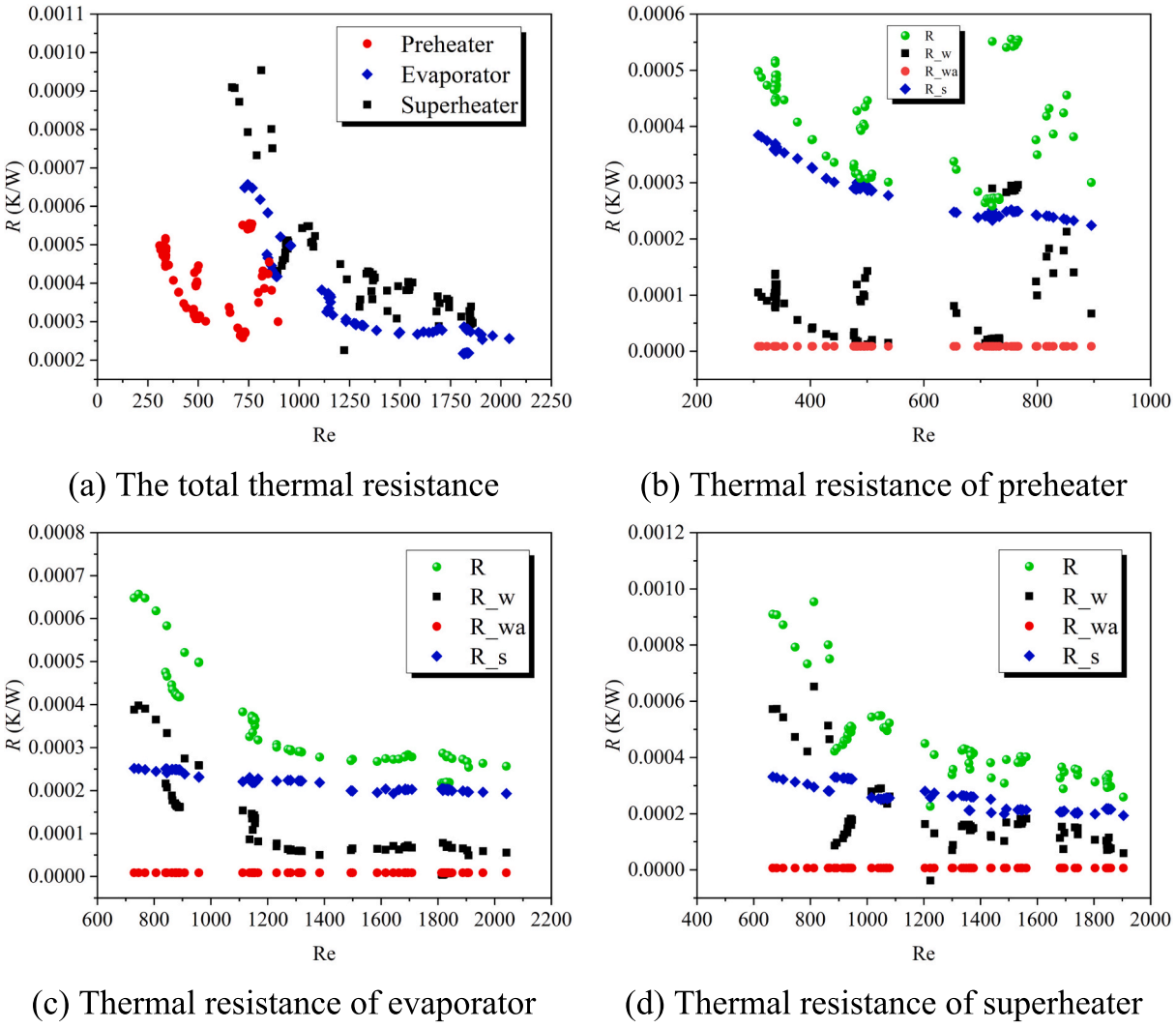

Fig. 10. The trend of thermal resistance in the main equipment varying with Re on the molten salt side.

3.3. Variation trends of parameters under special operating conditions

3.3.1. Failure of molten salt heaters and hot salt pumps

Fig. 11 presents the temperature on the steam/water and molten salt side of the main SGS equipment. During the operation of 1 h, the system experienced two special operating conditions, failure of the molten salt heater and stoppage of the hot salt pump. These conditions occurred both individually and in coupled periods. In Fig. 11, Ts_out represents the outlet temperature of the molten salt heater, showing a trend of initial decline, followed by a rise and then another decline, indicating three states: failure, normal operation, and temperature adjustment. The molten salt heater is responsible for heating cold salt to hot salt, replacing the steam-heated molten salt exchanger in the steam extraction system. Molten salt outlet temperature rapidly decreased upon heater failure at approximately 4–5 °C/min. Ts_in1 and Tw_out2 are the most sensitive to the heater failure. Due to residual heat in the heat exchanger walls, the molten salt temperature at the superheater inlet decreases relatively slowly, about 1–2 °C/min. The time interval from the heater restarting to the rise in molten salt inlet temperature is approximately 5 min. The outlet temperature of the superheated steam is the most sensitive to the heater, with a faster temperature drop of around 8–9 °C/min. As the molten salt temperature decreases, the cold salt absorbs heat from the tube walls, causing the steam outlet temperature to drop rapidly. In addition to the significant changes in the two variables above, the molten salt temperature at the evaporator inlet, the steam temperature at the evaporator outlet, and the water-side temperature at the superheater inlet are also affected. The observed trends show that when the molten salt heat exchanger fails, variables farther from the hot salt inlet experience the least impact. Water-side and molten salt-side temperatures of the superheater drop the fastest, while the evaporator shows minimal temperature changes due to the phase change point limitation. Similarly, the preheater exhibits no significant changes, thanks to the presence of the feedwater heater upstream.

In addition to salt heater shutdowns, the start/stop operation of the molten salt pump also has a notable impact on the system. Variable Qs1 in the Fig. 11 reflects the flow rate trend of the hot salt. It can be seen that the pump stopped four times, with each stoppage lasting about 120 s. Shaded areas in the figure represent the sudden temperature drops caused by the pump stoppage. After each stoppage, the molten salt temperature drops rapidly, with almost no delay, and the temperature of different heat exchangers decreases by around 5 °C. On the steam/water side, there is no significant temperature change during the pump stoppages due to two factors, the short duration of the stoppages and the presence of tube walls between the steam/water side and the molten salt side. The residual heat in the tube walls helps maintain the steam/water side temperature.

Fig. 12 shows the temperature of salt in the hot tank variation trend under particular operating conditions. Hot salt temperature does not exhibit significant changes with pump stoppages. The failure of the heater is the primary cause of temperature variation in the hot salt. Ts5,

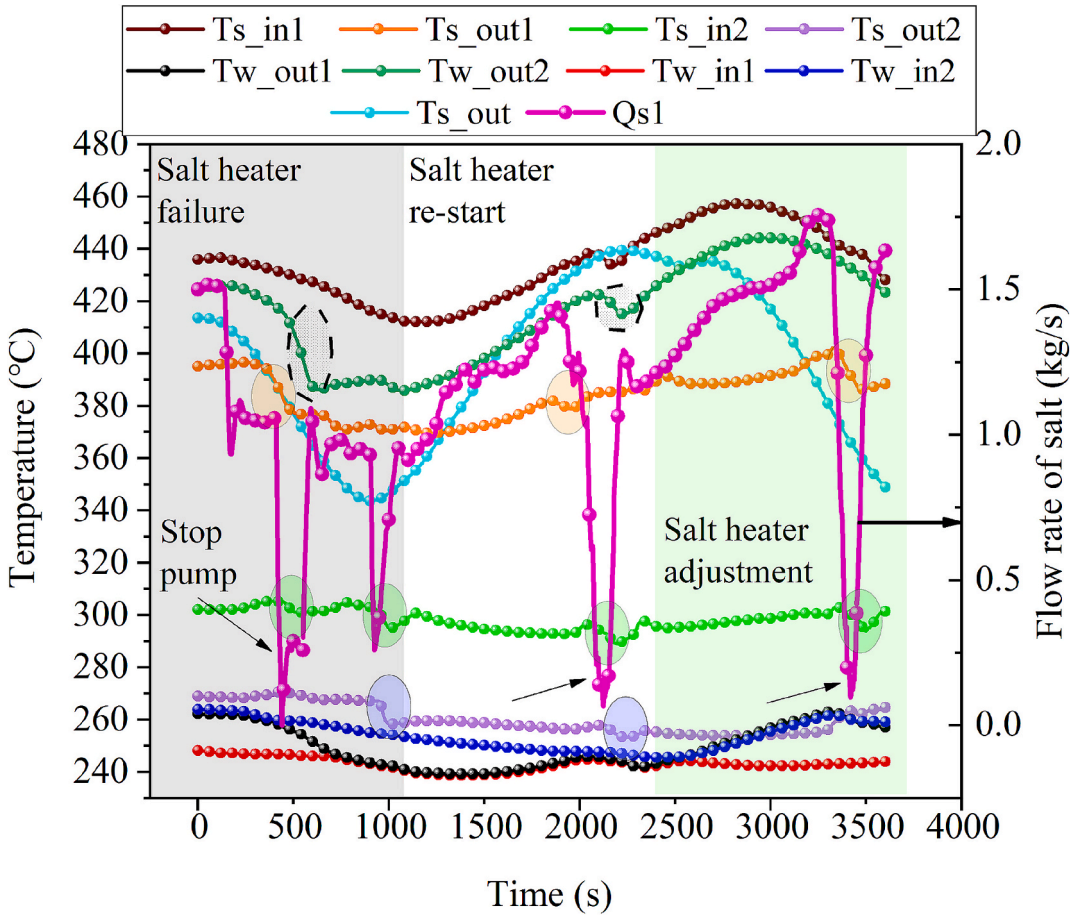

Fig. 11. Temperature trends at the inlets and outlets of the heat exchangers corresponding to the failure of the molten salt heater and the stoppage of the hot salt pump.

located at the bottom of the hot salt tank, is the first to come into contact with the hot salt from the heater, resulting in its temperature changing the fastest in response to the heater's condition. When the heater fails, cold salt continues to flow from the cold salt tank to the hot salt tank to maintain the internal temperature of the molten salt heater. This action leads to a temperature drop in the hot salt tank, with Ts4 and Ts5, located near the inlet, experiencing the largest temperature drop of about 20 °C. Once the molten salt heater resumes operation, there is a 5 min delay before the temperature at the bottom of the hot salt tank rises rapidly, increasing by 50 °C within 16 min. In the next stage, the power of the molten salt heater was reduced to conduct experiments at a salt temperature of 425 °C. Ts_out temperature dropped, leading to a corresponding decrease in the hot salt tank temperature. Overall, the hot salt temperature does not fluctuate due to molten salt pump failure but is closely related to the performance of the molten salt heater. When cold salt enters the hot salt tank, the maximum temperature drop rate within the tank is about 1–2 °C/min. Conversely, when hot salt enters the tank, the maximum temperature rise rate is 3–4 °C/min. These data provide a basis for verifying the thermal stress on the molten salt tank foundations and walls.

Figs. 13 and 14 focus on analyzing the impact of molten salt heater failure and pump stoppage on the temperature distribution within the cold salt tank and along the cold salt tank wall. As shown in Fig. 13(a) and (b), the cold salt temperature does not exhibit significant fluctuations due to either heater failure or pump stoppage. However, Fig. 14(a) and (b) reveal that the temperature along the cold salt tank wall drops rapidly due to changes in liquid levels caused by the pump stoppage. When the hot salt pump stops, cold salt continues to flow from the cold salt tank to the heater and subsequently into the hot salt tank to maintain the internal temperature of the heater. This action causes a gradual decrease in the liquid level within the cold salt tank. When the molten salt level falls below a specific measurement point, the temperature at that point drops rapidly by approximately 5 °C. In summary, most of the special operating conditions in the SGS system have some impact on the heat exchange system and the hot salt tank. However, the cold salt system remains largely unaffected by these conditions.

3.3.2. *Overpressurization of the superheater causes the safety valve to trip*

Fig. 15 illustrates the parameter variation trends under the superheater overpressure condition. Fig. 15(a) shows the operational parameters of the heat exchanger during the 1 h before and after the overpressure event, including pressure, temperature, and flow rate on both the steam/water and molten salt sides, with data recorded at 100 s intervals. The molten salt flow rate was the dominant factor in this overpressure incident. Between 1000 and 2800 s, the molten salt flow rate remained steady at 1 kg/s, allowing the system's pressure and temperature to remain stable. The outlet pressure of the feedwater heater reached 9.6 MPa, while the pressure inside the steam packet and superheater was around 9 MPa, remaining below the safety threshold of 10 MPa for the vessel.

At 2800 s, the hot salt pump was first shut down to increase pressure, allowing the molten salt to better fill the interior of the heat exchanger. It can be observed that the outlet temperatures of the superheated steam and molten salt and the system pressure rapidly decreased as the molten salt flow rate dropped. Subsequently, when the molten salt flow rate was increased to 2 kg/s, all parameters exhibited an upward trend, with the most notable change being a significant rise in the pressure within the heat exchanger system. Fig. 15(b) presents data collected every second

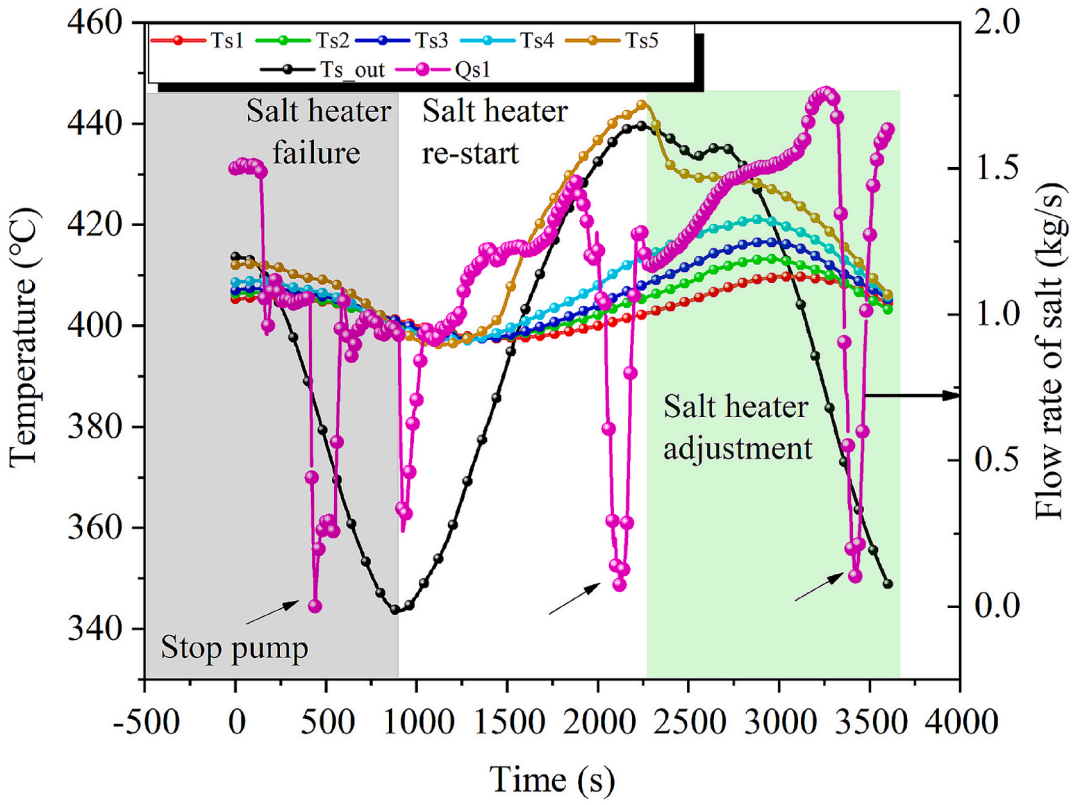

Fig. 12. Temperature trends of salt temperature in hot tank corresponding to the failure of the molten salt heater and the stoppage of the hot salt pump.

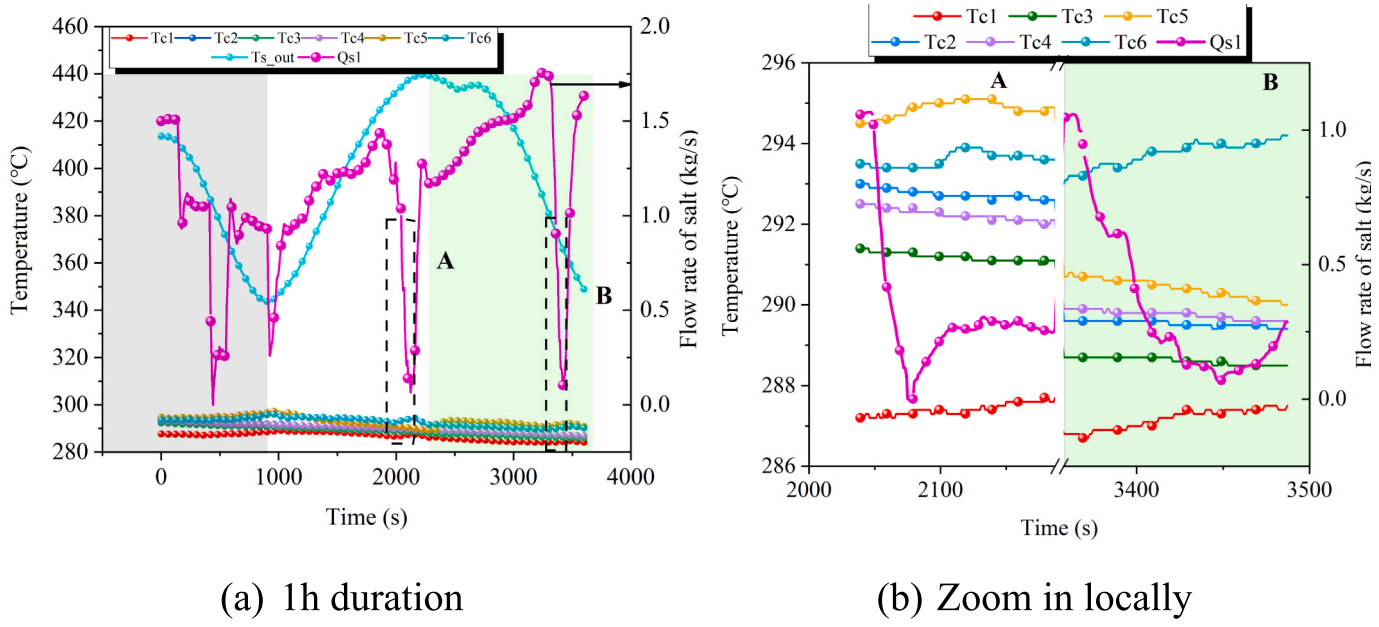

Fig. 13. Temperature trends of cold salt temperature corresponding to the failure of the molten salt heater and the stoppage of the hot salt pump.

after the 3000 s mark. It shows that the pressure in the heat exchanger system rose linearly at a rate of 0.6 MPa/min, reaching 9.7 MPa, approaching the 10 MPa set point of the safety valve. At 3215 s, the safety valve at the top of the superheater was triggered, causing the system pressure to drop rapidly by 5 MPa. 10 s after the safety valve activation, the hot salt pump was swiftly shut down to stop steam production. 15 s after the valve was triggered, it reset at the 5 MPa set point. As the closing action of the molten salt pump valve had not yet been fully completed, the system pressure slightly increased to 7.5 MPa due to the introduction of steam. After 75 s, the valve fully closed, causing the system pressure to rapidly decrease at approximately 0.4 MPa/min. The superheater was most sensitive to the safety valve release and molten salt pump failure, with the steam/water and molten salt sides experiencing rapid temperature drops. Outlet steam temperature decreased at up to 16 °C/min. Due to the feedwater heater and phase change points, the internal temperatures of the preheater and evaporator remained

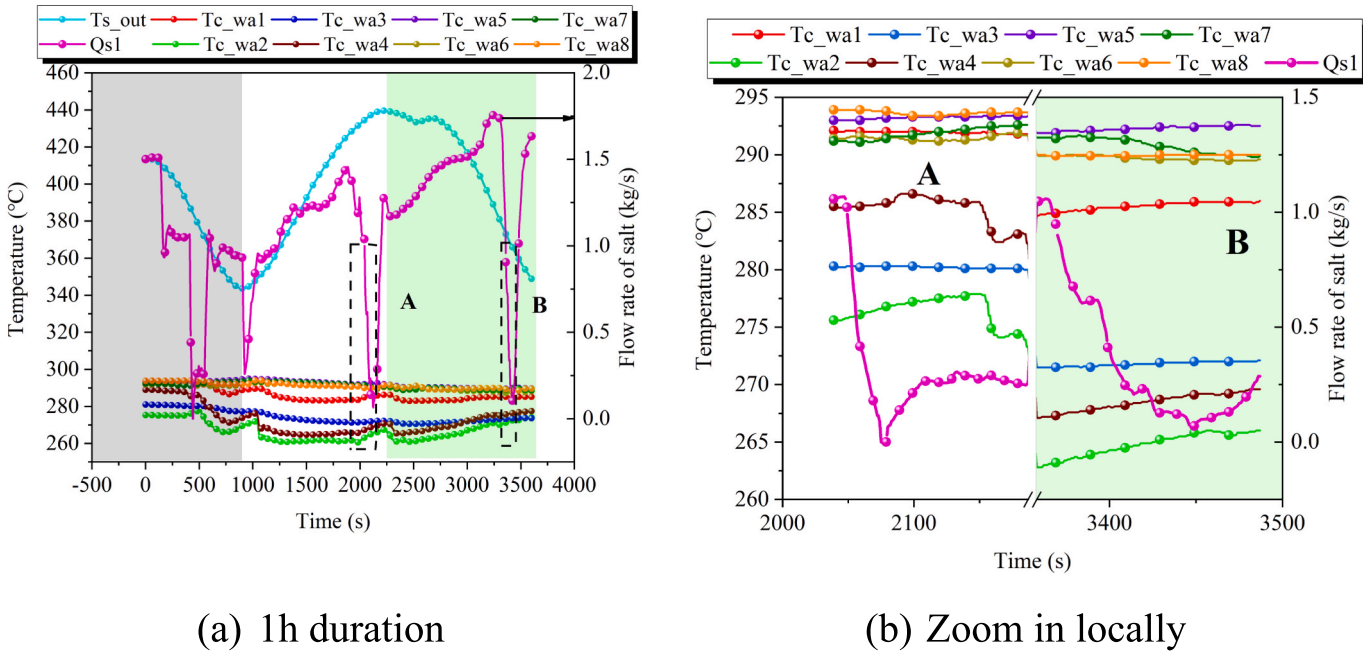

Fig. 14. Temperature trends of cold salt tank temperature corresponding to the failure of the molten salt heater and the stoppage of the hot salt pump.

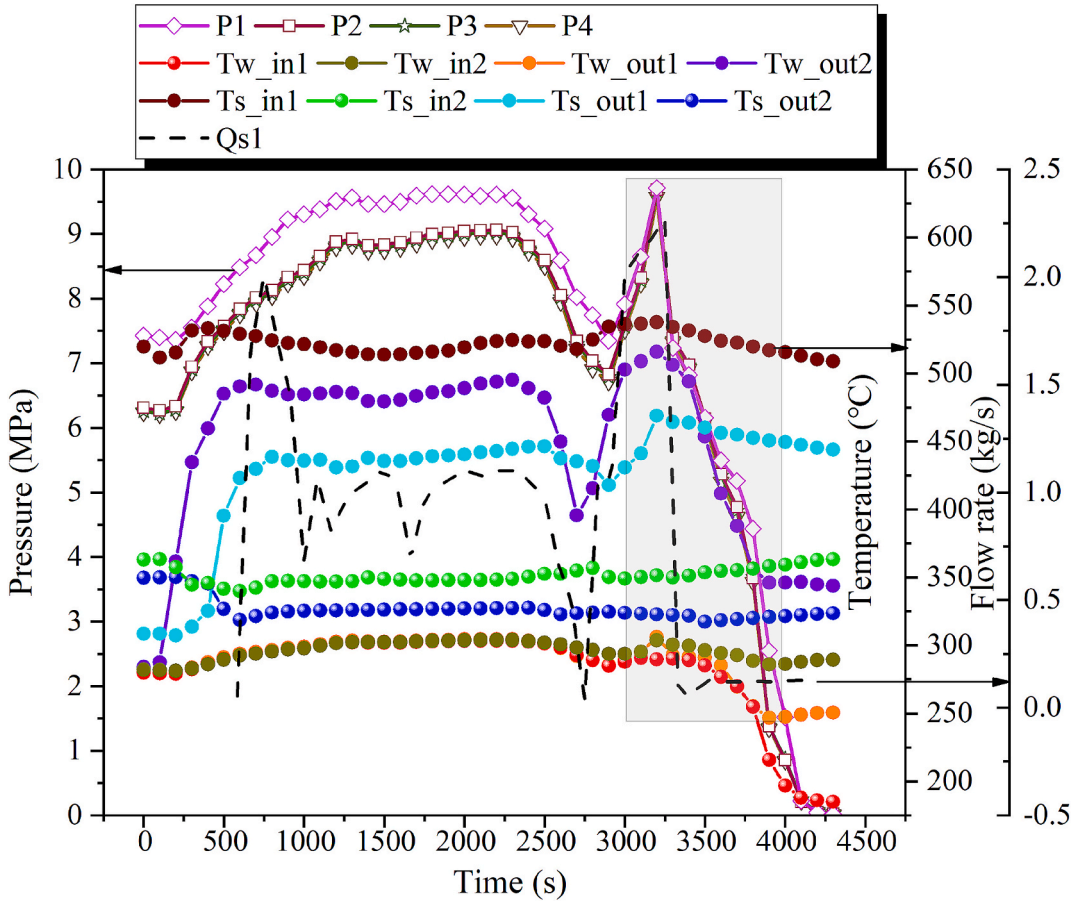

Fig. 15a. Trend of various parameters in the heat exchanger system under superheater overpressure conditions.

largely unaffected by external fluctuations. In summary, based on analyzing the failure of the molten salt heater, the stoppage of the molten salt pump, and the activation of the steam/water safety valve, it was identified that the evaporator is the most sensitive component. The rates and delays of superheated steam temperature and pressure drops under different accident scenarios were determined, providing data

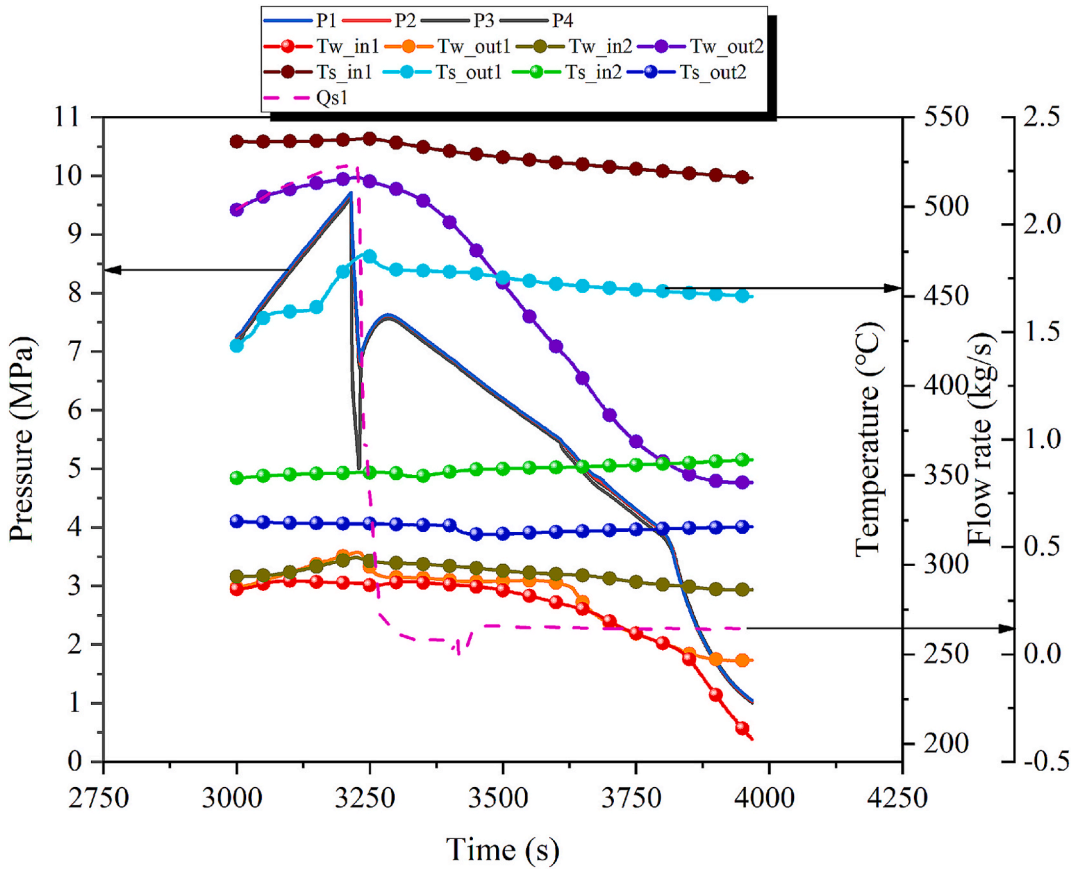

Fig. 15b. Enlarged view of the superheater safety valve release.

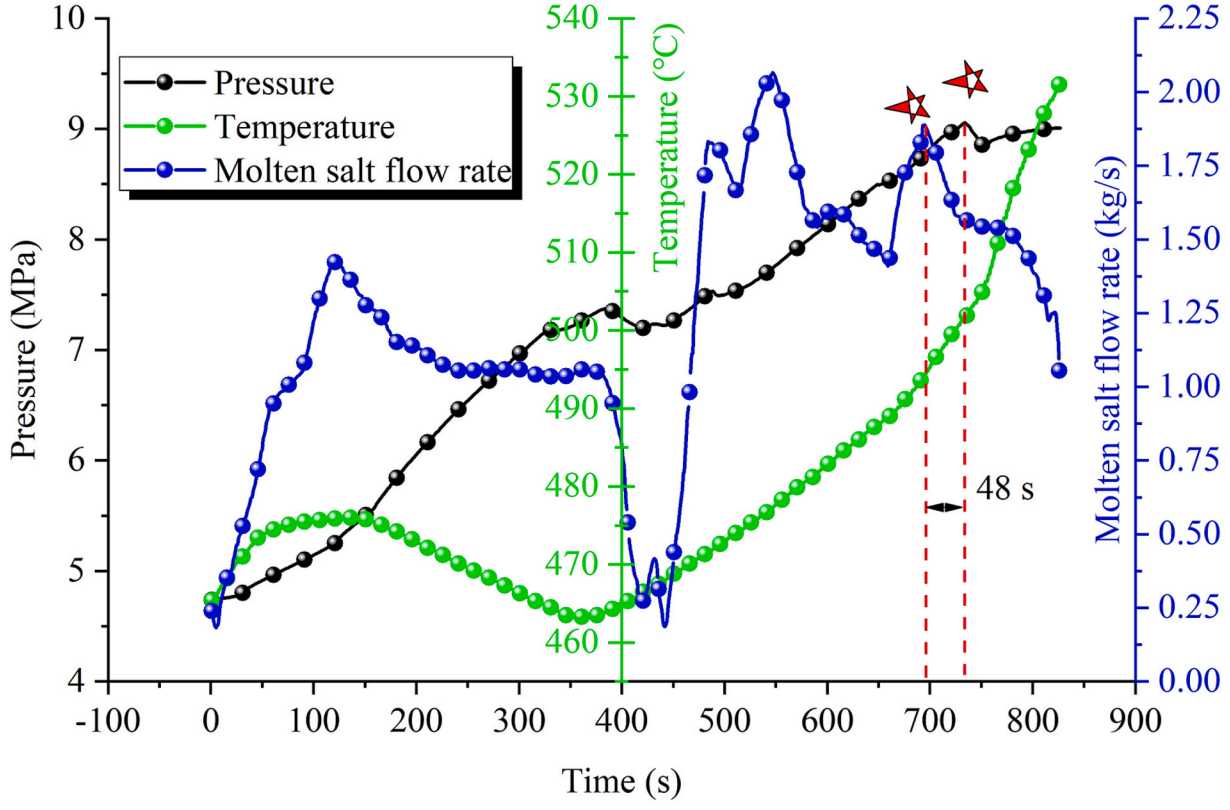

Fig. 16. Variation trends of the superheater parameters during normal operating conditions: Clarification of inertia time.

support for addressing unexpected issues in actual production.

3.4. Identification and prediction model of overpressure hazard parameters

Temperature and pressure are the two main variables that are difficult to control within the SGS. When the system temperature exceeds the upper limit allowed by the heat exchanger material, irreversible damage may occur to the tube walls, although this does not immediately lead to an accident. However, if the system pressure exceeds the limit, the safety valve will open immediately to ensure the safety of heat exchanger. Due to the complexity of the SGS and the flow-heat transfer process, the system has significant inertia, making real-time control commands ineffective in quickly and accurately managing system parameters. Therefore, understanding the pressure variation patterns and delay characteristics of the system is crucial for the normal operation and maintenance of SGS. Fig. 16 illustrates the pressure, temperature, and molten salt flow rate in the superheater during a particular operational condition. After 450 s, the molten salt flow rate increased from 0 to 2 kg/s, causing the pressure and temperature to rise rapidly. At 700 s, the operator noticed that the system pressure was rising rapidly and was about to reach the working pressure of the safety valve. In response, the molten salt flow rate was immediately reduced, and approximately 48 s later, the system pressure began to decrease. This phenomenon indicates that MW-level SGS has a delay of about 1 min, which imposes very strict requirements on pressure control. Operators must infer appropriate control actions based on the pressure variation trends under different operating conditions to ensure that the system does not exceed the pressure limit in the future. The predictive nature of this process places high demands on the operators, making the identification of overpressure hazard zones a key issue in supporting the system's automated operation. Fig. 17 presents the pressure variation trends of the superheater under different load changes. Using 48 s as the minimum warning time, the latest warning point for each operating condition can be determined. Load condition from 0 % to 80 % shows a rapid pressure increase, with significant system inertia, requiring the longest warning window. In contrast, the load condition from 60 % to 80 % exhibits the slowest pressure increase, requiring a smaller warning window. Blue region formed by connecting the warning points of different operating conditions and the safety valve's pressure limit represents the warning zone of the SGS. Once the system pressure enters this zone, superheater overpressure becomes inevitable. Therefore, it is crucial to prevent the pressure data from entering this region in actual operation.

Eq. (15) further clarifies the relationship between pressure and operational variables. By applying principal component analysis (PCA), 130 data points from the operation of the device were fitted, with the dependent variable being the superheater pressure and the independent variables being the molten salt flow rate, molten salt temperature, and feedwater flow rate. 130 data points were specifically chosen from transient conditions rather than steady-state or startup conditions because overpressure events typically occur during operational transitions. Independent variables were normalized to ensure the pilot test results could provide some guidance for MW-level concentrated solar power (CSP) plants. The design parameters for the pilot platform are as follows: molten salt flow rate of 2.5 kg/s, molten salt temperature of 565 °C, and feedwater flow rate of 0.42 kg/s, corresponding to 100 % operating load of hundred MW-level CSP plant. The actual operating parameters were normalized using the full-load operating parameters for fitting. These normalized values represent purely proportional relationships, meaning that Qs, T, and Qw all vary linearly. For example, when $Qs = 0.5$, the corresponding molten salt flow rate is 1.25 kg/s; when $T = 0.5$, the corresponding molten salt temperature is 282.5 °C; and when $Qw = 0.5$, the corresponding feedwater flow rate is 0.21 kg/s. In the model, Y indicates superheater pressure, MPa, Qs represents the

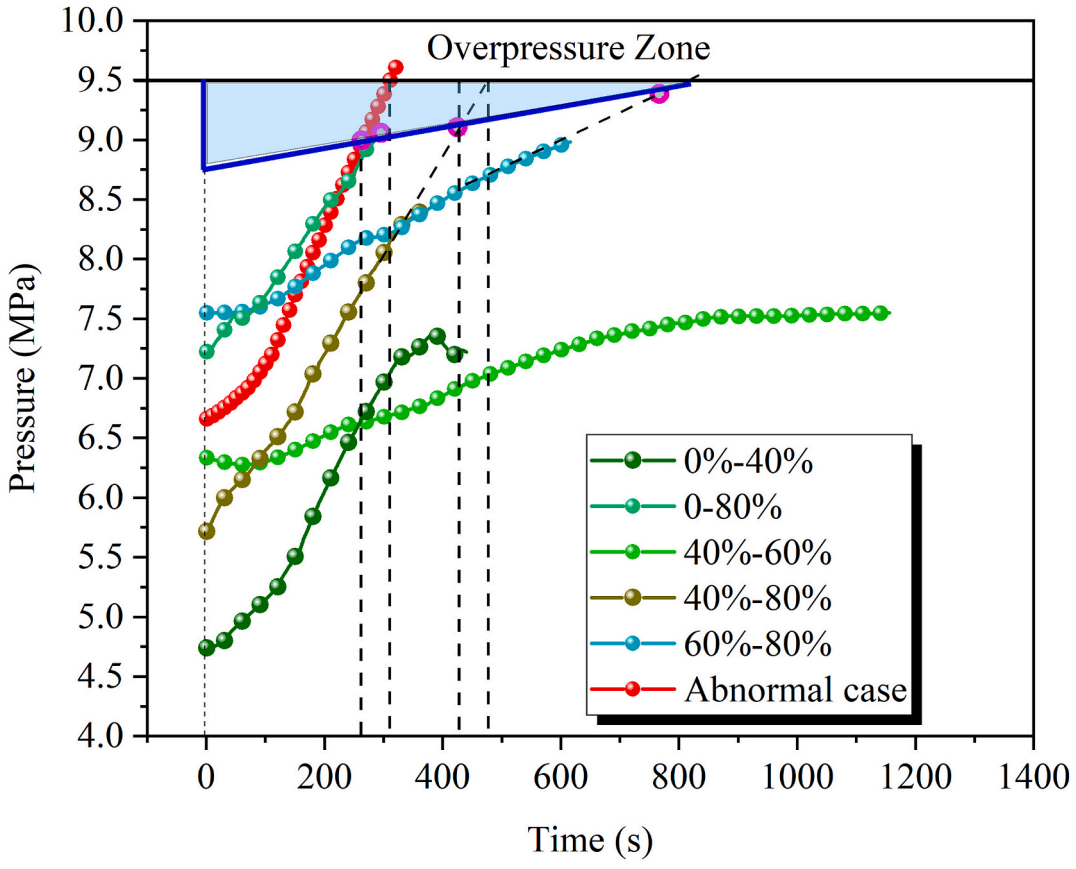

Fig. 17. Pressure variation trends of the superheater under different load changes.

molten salt flow rate, where a value of 1 corresponds to 2.5 kg/s; T represents the molten salt temperature, where a value of 1 corresponds to 565 °C; and Q_W represents the feedwater flow rate, where a value of 1 corresponds to 0.42 kg/s. Fig. 18 compares the predictions with the experimental values for the 130 data points, showing that the model achieves high predictive accuracy in the high-pressure range. The simulation error by dividing the difference between the predicted and experimental values by the experimental values was calculated to assess the model's accuracy. The final average error for the 130 predicted data points was found to be 16.5 %. Through both graphing and modeling methods, system pressure can be roughly predicted, providing a theoretical basis for operators to adjust controls.

$$Y = 1.93 + 8.18Q_s - 0.12Ts\_in - 0.56Q_w \quad (15)$$

4. Conclusion

This study was conducted on a MW-level pilot platform scaled down from a 100 MW solar thermal project, focusing on experimental investigations of crucial equipment such as the preheater, evaporator, and superheater. Research was carried out under system pre-start, normal, and accident conditions, leading to the following conclusions: (1) In the natural circulation packet operation mode, the steam/water side before the superheater must be preheated to the operating temperature before molten salt can be introduced. Significant fluctuations occur during the initial stage of salt introduction, causing severe thermal shocks to the tank walls. (2) When the molten salt flow rate increases from 1 kg/s to 2 kg/s and the temperature rises from 425 °C to 480 °C, the thermal efficiency of each heat exchanger decreases. The main reasons for this reduction in efficiency are the exacerbation of system heat loss and the deterioration of boiling due to high superheat. Corresponding efficiencies of the preheater, evaporator, and superheater are 40–55 %, 80–95 %, and 50–65 %, respectively. (3) The preheater and evaporator exhibit minimal thermal resistance, approximately 0.0004 °C/W. The steam side of the superheater and the molten salt side of the preheater account for 90 % and 70 % of the total thermal resistance, indicating that heat transfer enhancement measures can be applied to the steam and molten salt sides, respectively. (4) The failures of the molten salt heater, pump shutdown, and safety valve release significantly affect both the molten salt and steam/water sides of the superheater but have little impact on the preheater and evaporator. After heater failure, the temperature drop rate on the molten salt side of the superheater is about 1–2 °C/min, while the superheated steam temperature decreases by 8–9 °C/min. When the safety valve release is combined with the molten salt pump stoppage, the steam pressure decreases at a rate of 0.4 MPa/min, with the temperature drop rate reaching up to 16 °C/min. (5) The overpressure range and prediction model were obtained based on measured data and statistical analysis. These data provide criteria for rapid response and decision-making in emergency conditions.

CRediT authorship contribution statement

Xiang Liu: Writing – review & editing, Writing – original draft, Visualization, Validation, Software, Investigation, Formal analysis, Data curation. **Fengyongkang Wu:** Writing – review & editing, Data curation. **Xue Xue:** Writing – review & editing, Data curation. **Yifan Zhu:** Resources, Data curation. **Yaqiong Guo:** Funding acquisition, Conceptualization. **Mingbao Zhang:** Funding acquisition. **Hao Zhou:** Project administration, Conceptualization.

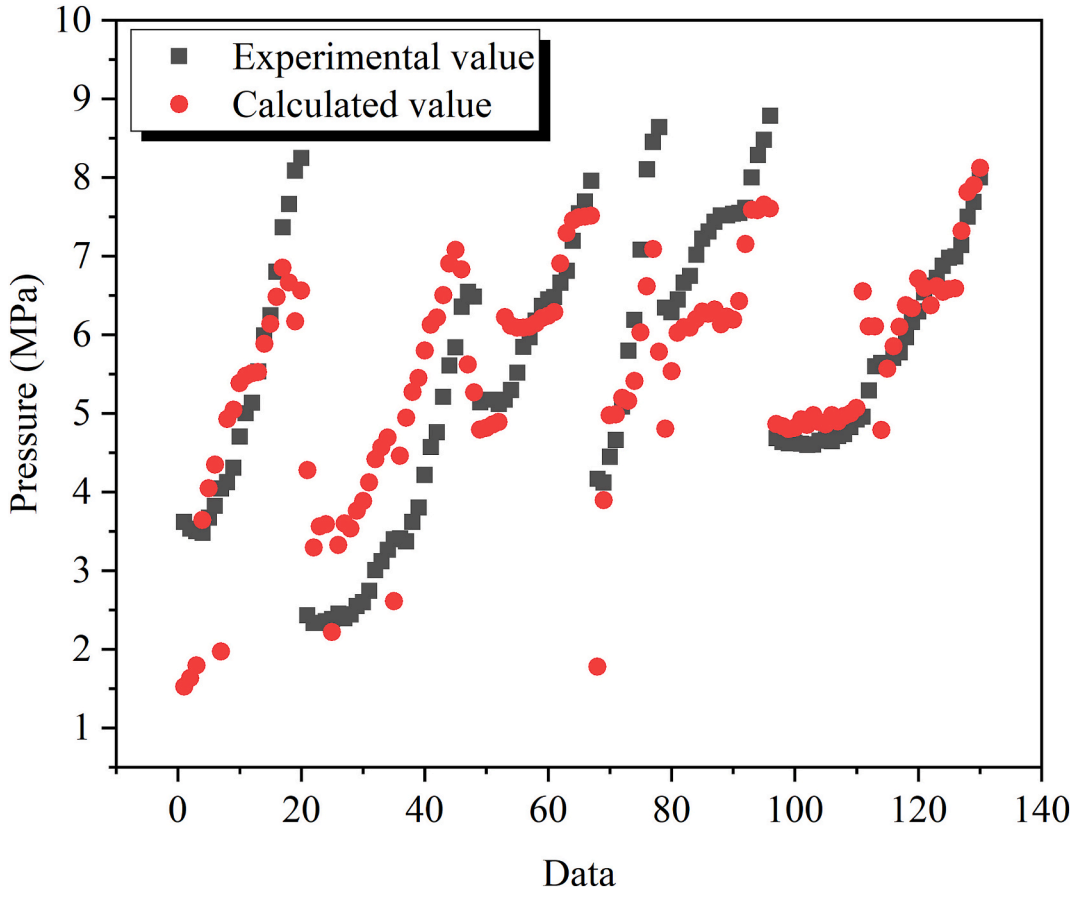

Fig. 18. The statistical prediction results of the superheater pressure.

Declaration of competing interest

The authors declare that they have no known competing financial interests or personal relationships that could have appeared to influence the work reported in this paper.

Acknowledgments

This work was supported by the Fundamental Research Funds for the Central Universities (2022ZFJH04).

References

[1] S.-Y. Yang, et al., Optical-thermal–mechanical comprehensive performance of the concentrating and collecting subsystem for the next-generation solar power tower based on heliostat field layouts optimization, Sol. Energy 275 (2024) 112604.
[2] C. Tripodo, S. Lorenzi, A. Cammi, Definition of model-based control strategies for the Molten Salt Fast Reactor nuclear power plant, Nucl. Eng. Des. 373 (2021) 111015.
[3] X. Liu, et al., Integration model and performance analysis of coupled thermal energy storage and ejector flexibility retrofit for 600 MW thermal power units, J. Clean. Prod. 428 (2023) 139337.
[4] Q. Yong, et al., Retrofitting coal-fired power plants for grid energy storage by coupling with thermal energy storage, Appl. Therm. Eng. 215 (2022) 119048.
[5] K. Hood, et al., Characterizing and improving the performance of molten-salt-steam heat exchangers in concentrating solar power plants, Energ. Conver. Manage. 315 (2024) 118721.
[6] Y. Qiu, et al., An experimental study on the heat transfer performance of a prototype molten-salt rod baffle heat exchanger for concentrated solar power, Energy 156 (2018) 63–72.
[7] Kirst, W.E., W.M. Nagle, and J.B. Castner, A new heat transfer medium for high temperatures.
[8] Hoffman, H.W. and S.I. Cohen. Fused salt heat transfer–part III: forced-convection heat transfer in circular tubes containing the salt mixture nano$sub 2$-nano$sub 3 $-kno$sub 3$. 1960.
[9] K. Abramova, et al., Molecular dynamics study of the temperature dependence of viscosity and thermal conductivity of molten salts FLiNaK and FLiNaK with LaF3 or NdF3, J. Mol. Liq. 407 (2024) 125154.
[10] S. Zhang, X. Sun, Mixed convective and radiative heat transfer of LiF-BeF2-ThF4-UF4 in a vertical circular tube, Ann. Nucl. Energy 185 (2023) 109706.
[11] Silverman, M.D., W.R. Huntley, and H.E. Robertson, Heat transfer measurements in a forced convection loop with two molten-fluoride salts: LiF–BeF/sub 2/–ThF/sub 2/–UF/sub 4/ and eutectic NaBF/sub 4/–NaF. 1976.
[12] Á.G. Fernández, et al., Compatibility of alumina forming alloys with LiNO3-containing molten salts for solar thermal plants, J. Storage Mater. 48 (2022) 103988.
[13] S. Zhang, X. Sun, E.E. Dominguez-Ontiveros, Numerical study on convective heat transfer and friction characteristics of molten salts in circular tubes, Ann. Nucl. Energy 142 (2020) 107375.
[14] J. Steinbrecher, et al., Stabilization of Solar Salt at 650 °C – Thermodynamics and practical implications for thermal energy storage systems, Sol. Energy Mater. Sol. Cells 258 (2023) 112411.
[15] A.K. Srivastava, et al., Heat transfer and pressure drop characteristics of molten fluoride salt in circular pipe, Appl. Therm. Eng. 61 (2) (2013) 198–205.
[16] F. Yao, Q. Bi, X. Dong, Convective heat transfer of high temperature molten salt flowing across tube bundles of steam generator in a solar thermal plant, Appl. Therm. Eng. 141 (2018) 858–865.
[17] S. He, et al., Convective heat transfer of molten salt outside the tube bundle of heat exchanger, Exp. Therm Fluid Sci. 59 (2014) 9–14.
[18] Y.-L. He, et al., Experimental investigation on turbulent heat transfer characteristics of molten salt in a shell-and-tube heat exchanger, Appl. Therm. Eng. 108 (2016) 1206–1213.
[19] B.-C. Du, et al., Convective heat transfer of molten salt in the shell-and-tube heat exchanger with segmental baffles, Int. J. Heat Mass Transf. 113 (2017) 456–465.
[20] J. Qian, et al., Performance of a gas cooled molten salt heat exchanger, Appl. Therm. Eng. 108 (2016) 1429–1435.
[21] Y.S. Chen, et al., Experimental study of heat transfer enhancement for molten salt with transversely grooved tube heat exchanger in laminar-transition-turbulent regimes, Appl. Therm. Eng. 132 (2018) 95–101.
[22] L. Jianfeng, et al., Convective heat transfer of high temperature molten salt in transversely grooved tube, Appl. Therm. Eng. 61 (2) (2013) 157–162.
[23] Z. Ying, et al., Convective heat transfer of molten salt-based nanofluid in a receiver tube with non-uniform heat flux, Appl. Therm. Eng. 181 (2020) 115922.
[24] C. He, et al., Heat transfer and thermal performance of two-stage molten salt steam generation system, Appl. Energy 204 (2017) 1231–1239.
[25] Y. Zou, et al., Heat transfer performance of U-tube molten salt steam generator, Int. J. Heat Mass Transf. 160 (2020) 120200.
[26] J. Lu, et al., Experimental thermal performance study of molten salt steam generator-superheater with saturated water, Int. J. Heat Mass Transf. 168 (2021) 120884.
[27] X. Dong, et al., Experimental investigation on the shell-side heat transfer performance of molten salt steam generator, Int. J. Heat Mass Transf. 158 (2020) 119991.
[28] X. Dong, et al., Experimental investigation on the heat transfer characteristics of molten salt to subcooled boiling water, Int. J. Heat Mass Transf. 159 (2020) 120120.
[29] X. Xue, et al., 1.05 MW molten salt furnace experimental investigation of full-conditional thermal energy storage for the transfer and storage of waste heat from blast furnace gas, Renew. Energy 231 (2024) 120955.
[30] H. Nemati, et al., Chapter 11 - Logarithmic mean temperature difference, in Fundamentals of Industrial Heat Exchangers, H. Nemati, et al., Editors. 2024, Elsevier. p. 165-177.
[31] S.J.M. Cartaxo, F.A.N. Fernandes, Counterflow logarithmic mean temperature difference is actually the upper bound: a demonstration, Appl. Therm. Eng. 31 (6) (2011) 1172–1175.
[32] B. Sun, et al., Heat transfer characteristics of high-temperature, Nucl. Tech. 38 (03) (2015) 72–76.
[33] E.N. Sieder, G.E. Tate, Heat transfer and pressure drop of liquids in tubes, Ind. Eng. Chem. 28 (12) (1936) 1429–1435.